Architecture and flexibility of native kinetochores revealed by structural studies utilizing a thermophilic yeast

Daniel J. Barrero

A dissertation

submitted in partial fulfilment of the requirements for the

degree of

Doctor of Philosophy

University of Washington

2024

Reading Committee:

Sue Biggins, Chair

Chip Asbury

Trisha N. Davis

Program Authorized to Offer Degree:

Molecular and Cellular Biology

University of Washington

Abstract

Architecture and flexibility of native kinetochores revealed by structural studies utilizing a thermophilic yeast

Daniel J. Barrero

Chair of the Supervisory Committee:

Sue Biggins

Division of Basic Sciences, Fred Hutchinson Cancer Center and Howard Hughes Medical Institute

In order to propagate, cells must be able to duplicate and faithfully segregate their genetic information. Eukaryotic chromosome segregation requires kinetochores, multi-megadalton protein machines that assemble on the centromeres of chromosomes and mediate attachments to dynamic spindle microtubules. Kinetochores are built from many complexes, and understanding how they are arranged is key to understanding how kinetochores perform their multiple essential functions. However, an integrated understanding of kinetochore architecture has not yet been established. To address this we turned to a thermotolerant yeast, *Kluyveromyces marxianus,* in the hopes we would be able to purify kinetochores stable enough for structural studies. We were able to purify kinetochores from *K. marxianus* and study them by electron microscopy, cryo-electron tomography and atomic force microscopy. The kinetochores are extremely large, flexible assemblies that exhibit features consistent with prior models. We

assigned kinetochore polarity by visualizing their interactions with microtubules and locating the microtubule binder Ndc80c.

We were also surprised to find two distinct classes of kinetochores, doublets and singlets. Suspecting that the doublets might indicate a regional centromere, we further interrogated their function and origin. We found that while the doublets could account for the high strength of its' kinetochores, *K. marxianus* in fact utilized a point centromere much like *Saccharomyces cerevisiae*. This work shows that isolated kinetochores are more dynamic and complex than what might be anticipated based on the known structures of recombinant subassemblies and provides the foundation to study the global architecture and functions of kinetochores at a structural level.

Acknowledgements

There is a large company of people, professionally and personally, who deserve thanks. I'd like to start by thanking the many great professors at the University of Redlands, whose passion for not just teaching, but connecting with students is evident. For the sake of space I'll only highlight two of them, Drs. Bill Casale and Caryl Forristall. Bill's cell biology class was pivotal for me because it reminded me of how wild it is that any biological process works at all. Caryl's guidance as an advisor was invaluable, and she continued to offer guidance after my graduation.

I would also like to thank Drs. Joseph (Jody) Puglisi and Elisabetta (Betta) Viani-Puglisi. They hired me soon after I graduated, despite my not having particularly extensive research experience or coming from a big-name school. They also encouraged me to go to my first conference, a small course on biophysics in Erice, Italy. This was the first time I was surrounded by early career scientists and despite giving possibly the worst presentation of my career (seven years later it still holds the crown), the encouragement and enthusiasm I felt from everyone went a long way in convincing me to pursue a career in research. Jody and Betta always stressed the importance of doing rigorous, high-quality work, and their support and encouragement helped me believe that I could be successful in any of the best research institutions in the world. I'd also like to thank Dr. Kevin Larsen, my at-the-bench mentor during my time in the Puglisi lab. He was a graduate student when I joined the lab and taught me almost every protocol I would use for the next two years, and now as a graduate student myself I more fully appreciate the time and patience he provided for me.

Special thanks also go to my advisors, Drs. Chip Asbury and, especially, Sue Biggins. Anyone who interacts with Chip for more than a minute will be able to appreciate the wonder with which he approaches science. It both infectious and refreshing. He also has an incredibly keen analytical eye for science. Personally if I could run grants, papers, and presentations by

Chip forever I would, because I know if it can make it past him without complaints it will make it past most anybody.

Sue has created an excellent home lab to do science in. She has given me tremendous independence with which to pursue my project. I've heard it said that a great mentor may not always have the answers but will always try their best to put you in front of people who do. Sue has done this for me since day one. Sue has an incredible depth of knowledge in our field, but my project has always been slightly outside the standard wheelhouse of our lab. Sue has always been the first to admit when she was not an expert in a technique and worked hard to make connections with people that were. This is largely what made my project possible and led to great collaborations. She is continually trying to improve as a mentor and is always willing to use her position to make things better for her trainees.

Finally, I'd like to thank everyone in the Biggins lab. They're fantastic. They are all not just willing to help, but actively want to help each other. It is wonderful to be in a group where everyone wants each other to succeed.

Now for the more personal acknowledgements. There are many people outside the science world who I'd like to thank. I'd like to thank my dentist, for fixing the tooth that I cracked from stress-clenching my teeth in the final year of graduate school. I'd also like to reprimand my dentist for asking me about my life in the midst of anesthetizing my mouth. Thank you to all my friends stayed in contact with me as I disappeared into the cave of graduate school, where my admittedly already bad habit of slow responses was magnified. I'd like to thank my Brazilian jiu jitsu friends. No matter how great or awful my day was, class started at 7:15 pm and for the following hour and a half I had to be fully present in the moment, lest one of my good buddies catch me in a choke or joint lock. In that sense jiu jitsu became an active meditation for me. Similarly I'd like to thank my cat who's perpetually looking for either a lap to sleep on or a buddy to mess around with.

Some of the biggest thanks have to go to my family. My family came to the U.S. from Venezuela when I was a toddler, in search of a better life like so many others. That decision to move to a new country, barely knowing the language and knowing for certain that you are leaving most if not all of your support system behind is a courageous act I'm not sure I'd be able to replicate. Luckily we were able to find a couple other Venezuelan families who made the same move, and were able to form one super-family that I am very proud of. I'd like to thank my parents for fostering my curiosity and encouraging me to ask questions, even in my younger years at the cost of their sanity and sleep. I'd also like to thank my little brother. We've been tight since the day he was born, and I hope that never changes. His ability to show up authentically and whole heartedly is something I will always strive to emulate. Finally, I'd like to thank my partner Marielle. She has offered such great love and support, and we have built a delightful little life together. I love you all and hope to make you proud.

Table of Contents

Chapter 1: Introduction

1.1 Mitosis is a critical process for life

No lineage of living organisms can continue to exist without the ability to propagate its genetic information to the next generation. Across every domain, from archaea to prokaryotes to eukaryotes, the overall strategy appears the same; a single cell will duplicate its genetic material, segregate the copies to distinct areas which will then become daughter cells, and finally sever those two cells from each other[1,2]. In eukaryotes the process by which duplicated DNA is separated leading to the formation of two daughter cells is mitosis. Mitosis has been appreciated since the early days of microscopy, notably in Walther Flemming's now classic illustrations of dividing cells from 1882[3]. In fact it was Flemming who coined the term 'mitosis' from the ancient Greek μίτος meaning 'thread', referring to the condensed, thread-like chromosomes[3,4]. Though there are variations between eukaryotic lineages, the major players of mitosis remain well conserved. Generally, a cytoskeletal mitotic spindle is formed with opposing spindle poles. This spindle then reaches out and contacts chromosomes, an interaction mediated by kinetochores. These kinetochores then enable the chromosomes to be pulled to the correct end of the cell and allow for cell division to progress. The budding yeast *Saccharomyces cerevisiae* has proven to be an extremely useful system for studying mitosis thanks to its simplified mitotic machinery and powerful genetics. In the following chapters I will dive into greater detail on chromosome segregation focusing mainly on *S. cerevisiae* but expanding on other organisms as well.

1.2 The mitotic spindle

Chromosome segregation is mediated by interactions between the mitotic spindle and kinetochores, which assemble directly on chromosomes. The core components of mitotic spindles are microtubule organizing centers (MTOCs), known as the centrosomes in animals

and spindle pole bodies (SPBs) in yeast [5]. These two organelles are structurally distinct, however they share some key components such as the microtubule nucleating protein γ-tubulin[6,7]. The SPB is embedded within the nuclear membrane and remains present throughout the cell cycle[8]. It is composed of 5 layers, 3 of which are highly organized and densely packed making them easily identifiable by electron tomography. Because of this the SPB is often referred to as a trilaminar disk[9]. These three layers are the outer, central, and inner plaques, with the outer and central plaques connected by the intermediate layers IL1 and IL2[9]. The core of the SPB is the central plaque, which is formed by a hexagonal lattice of the protein Spc42[10] . Towards the cytoplasm, the C-terminus of Spc42 binds the IL1 and IL2 proteins Cnm67 and Nud1, respectively. Nud1 then binds the protein Spc72, the adapter for the γ-tubulin complex (γ-TuSC), which nucleates cytoplasmic microtubules important for appropriately positioning the nucleus within the cell[7,8]. Towards the nucleoplasm the N-terminus of Spc42 binds the C-terminus of Spc110, a long coiled-coil that protrudes out of the central plaque[11,12]. The proteins Spc29 and calmodulin are also bound by the C-terminus of Spc110[7].

Like Spc72, the N-terminus of Spc110 binds γ-TuSC which nucleates spindle microtubules[7]. γ-TuSC is composed of γ-tubulin and the adapter proteins GCP2 and GCP3. These adapters each bind one copy of γ-tubulin, forming a Y shape with γ-tubulin at each arm, and GCP2/3 reaching back to contact Spc72 or Spc110 for the outer or inner plaque respectively[7,13]. Oligomers of γ-TuSC come together to form a cone, presenting the γ-tubulin at the wider end with the correct spacing to initiate microtubule nucleation from αβ-tubulin dimers[7]. The cone of γ-TuSC can alternate between an open and closed state, with the closed state being a more powerful nucleator providing a mechanism of allosteric regulation[14]. The activity of γ-TuSC on the cytoplasmic and nuclear sides is likely differentially regulated, as the inner plaque generates between 2 to 5 fold more microtubules, with some estimates being as high as 10 fold[15-17].

Duplication of the SPB occurs in 3 steps: half bridge extension and satellite formation, maturation, and insertion. A key player in this process is a thin structure called the half bridge, visible as an electron dense region on the inner and outer nuclear membrane[9]. The half bridge is composed of a single sheet of the protein Sfi1, a long repetitive helical protein[18]. To initiate SPB duplication in late anaphase the half bridge elongates to a full bridge which will connect the original mother SPB and new daughter SPB[8,19]. This elongation is dependent on the loss of Cdk1 phosphorylation[20]. The elongated Sfi1 sheet is then able to bind the core components of the SPB central plaque (Spc42 & Spc29), a process known as satellite deposition. How the satellite SPB is recruited to the full bridge is unclear, however it appears to be dependent on activity of Mps1 kinase[20].

During SPB maturation in G1 the proteins Nud1 and Cnm67 are bound to the central plaque to create intermediate layers IL1 and IL2, respectively[21]. To insert into the nuclear membrane, the mature SPB requires a nuclear envelope pore, the formation of which is thought to be driven by proteins that encourage high membrane curvature[22]. Once the daughter SPB has been inserted into the nuclear envelope it must separate from the mother to form a bioriented mitotic spindle. Initial release of the daughter is thought to occur by phosphorylation of Sfi1 by Cdk1, which separates the full bridge into two half bridges, one attached to each SPB[23]. For mitosis to progress, the SPBs must move away from each other, eventually forming a fully bioriented spindle. This is achieved mainly through the interactions between the microtubules of each SPB and crosslinking molecular motors. Minus-end directed motors such as Kar3/Cik1 (Kinesin-14 in humans) bind a microtubule as cargo and walk along a microtubule from the opposite SPB, thus aligning the two as an antiparallel bundle[24]. After this alignment the plus-end directed motor Cin8 (kinesin-5 in humans) crosslinks antiparallel microtubules and generates an expanding force by walking toward microtubule plus-ends, separating the SPBs into an elongated, bioriented spindle[24]. There is also evidence that non-enzymatic diffusible

crosslinkers aid in this process by generating force through entropic expansion along microtubule lattices, and later in mitosis inter-kinetochore stretching also plays a role[25,26].

The major source of mechanical energy for chromosome segregation comes from the microtubules themselves. Microtubules are tube like polymers composed of repeats of α and β tubulin dimers arranged head to tail[27,28]. A key feature of microtubules is dynamic instability, the ability to go through continual cycles of growth and shortening by the addition and subtraction of these tubulin heterodimers[29]. Dynamic instability is an energy consuming process that allows microtubules to explore large areas inside the cell, important for searching for and capturing chromosomes[30]. The GTP cap model can largely explain this behavior. Soluble tubulin heterodimers bind GTP before incorporation into the microtubule lattice, where the GTPase activity of tubulin is activated and GTP is hydrolyzed to GDP. This creates a microtubule where the majority of the lattice is GDP bound, while the tip contains GTP. It is proposed that this cap stabilizes the entirety of the filament[29]. In this model the GDP lattice is inherently unstable, and once the GTP cap is lost the microtubule begins to depolymerize (termed a catastrophe event) until it is entirely disassembled or the GTP tip is stochastically reestablished (termed a rescue event)[31].

Two models exist to explain the inherent instability of the GDP lattice – the allosteric and lattice models. In the allosteric model the hydrolysis of GTP to GDP creates a conformational change in the tubulin heterodimer. However, because this hydrolysis occurs in the lattice where tubulin subunits are locked in, the conformational change results in accumulated strain within the lattice itself[31]. Recent support for this model comes from cryo-EM studies demonstrating that GTP bound tubulin dimers have a more straight conformation than GDP bound[32]. In contrast, the lattice model instead proposes that both the GTP and GDP bound states of tubulin heterodimers maintain the same conformation and that GTP hydrolysis instead affects lattice interactions in a different way such as weakening lateral bonds[31]. The lattice model is supported

by tubulin heterodimer structures determined by x-ray crystallography, however with the caveat that these structures were solved in the presence of polymerization inhibiting factors[33,34].

In any case, the sustained connection between these dynamic tips and kinetochores is essential for chromosome segregation. In the following chapters I will discuss the assembly and architecture of the kinetochore, as well as how it is thought to interact with microtubule tips.

1.3 The kinetochore

1.3.1 The centromere

Eukaryotic cells use massive protein machines called kinetochores to harness the movement of dynamic microtubules to segregate chromosomes[35-37]. The kinetochore assembles on specific regions of DNA called centromeres. In *S. cerevisiae* the centromere consists of a ~125-bp region consisting of three conserved centromere defining elements (CDEs I, II, and III)[38-40]. CDEI and CDEIII are shorter (8 and 26-bp respectively), while CDEII is an AT rich ~80-bp stretch[38]. These three sequences mark the position for deposition of the H3 histone variant Cse4[41,42]. Centromere binding factors (Cbf) 1 and 3 bind to CDEI and CDEIII and are key for the formation of the Cse4 nucleosome[43]. Despite some controversy, the most widely accepted model of the centromere is a conventional octameric nucleosome containing two copies of Cse4, H2A, H2B, and H4[44]. The structure of the Cse4 nucleosome has been solved by cryo-EM, however it is not wrapped tightly by centromeric DNA and as such structures only exist bound to variations of Widom 601 DNA or through antibody stabilization of the nucleosome core particle[43,45]. Interactions between the Cbf3 complex, Cbf1, and Cse4 itself are crucial for the stable formation of the centromeric nucleosome[43,46].

1.3.2 The inner kinetochore

The key inner kinetochore unit is the constitutive centromere associated network (CCAN) which binds directly to the centromere[47]. This 14 member network forms an arch-like structure and can be broken down into 4 groups: Mif2, Ctf19, and Cnn1c. Mif2 is a long and largely disordered protein that directly contacts the Cse4 nucleosome, the Ctf19 complex members Ame1 and Okp1, and the outer kinetochore through the MIND complex[48]. Because of this it is sometimes referred to as the blueprint of the kinetochore.

The Ctf19 complex is composed of the proteins Mcm16, Mcm22, Ctf3, Iml3, Chl4, Mcm21, Ctf19, Okp1, Nkp1, Nkp2, and Ame1, and is the bulk of the CCAN[49,50]. The Ctf19 subcomplex Chl4/Iml3 directly binds to the L1 loop of Cse4, however it has proven difficult to see this interaction in structures of complete CCANs bound to Cse4 nucleosomes[51]. There is also evidence for the binding of Cse4 directly by Ame1[52,53]. Instead, structures of complete CCAN complexes have been able to resolve the arch of Chl4/Iml3 interacting with the partially unwrapped DNA of the nucleosome[49,54]. Cnn1c (proteins Cnn1 and Wip1) interact with Ctf3 and also has conserved DNA binding residues[55-57]. Cnn1c may also play a role in the arrangement of two CCANs on the centromeric nucleosome, though it remains one of the most difficult members of the complex to resolve.

Two copies of CCAN are present at the kinetochore, though their arrangement around the centromeric nucleosome is still an active area of study[58]. Attempting to symmetrically sandwich each CCAN around the Cse4 nucleosome leads to significant steric clashes[50,54]. A potential solution has been proposed based on solved structures of CCAN bound to centromeric DNA largely without contacting the nucleosome directly. In this model one CCAN binds as previously established, with the DNA binding groove of Chl4/Iml3 contacting the partially unwrapped DNA of the nucleosome and Cnn1c swung open to accommodate the nucleosome within the arch[54]. This is referred to as the non-topological configuration[49]. A second CCAN,

referred to as topologically entrapped, then can bind such that the CDE1 element is threaded through the arch and the Cnn1c is swung closed, fully entrapping the DNA. This positions the topological CCAN directly behind the CBF1 complex, which is still able to bind the CDE1 element, and positions the topological CCAN sufficiently close to the nucleosome to remain linked by Mif2, although this linkage could not be visualized due to the high flexibility of Mif2[49]. Though appealing, this model does not recapitulate the previously established interaction between Cse4 and Chl4. It is also missing the key Cbf3c component Ndc10, which is expected to remain associated with the kinetochore throughout the cell cycle. Additionally Cnn1c remains poorly resolved. Finally, to create a complex stable enough for cryo-EM almost the entirety of CDEII was replaced with the much more stabling wrapping W601 sequence. Thus though these structures and the resulting models are exciting advances, the arrangements of the CCANs in the kinetochore requires continued investigation.

1.3.2 The outer kinetochore

Mif2, Ame1, and Cnn1 create the connections to the outer kinetochore[59-64]. All of these proteins achieve this through unstructured tails. Mif2 and Ame1 are essential, and contact the outer kinetochore complex MIND, while Cnn1c is nonessential and directly contacts the outer kinetochore complex Ndc80c. MIND (proteins Dsn1, Mtw1, Nsl1 and Nnf1) is a roughly 22 nm heterotetramer with intertwined helices that form a long Y shape, with the c-termini gathered at the base and the n-termini gathered in the two heads[59]. The Ame1 and Mif2 binding sites are located on head I, however these sites can be occluded by head II creating a regulatory autoinhibition mechanism that can be relieved by Ipl1 phosphorylation[59]. An additional level of regulation occurs at Mif2, which is in an autoinhibited state until binding of Cse4 releases the N-terminus to bind MIND[65]. The binding of these two proteins to MIND is mutually exclusive, as they share a binding motif on Mtw1[65].

MIND recruits Ndc80c (proteins Ndc80, Nuf2, Spc24 and Spc25), the major microtubule binder, through the c-terminus of Dsn1 [59,61]. Ndc80c is also directly recruited by Cnn1, and though this recruitment is non-essential in yeast it becomes essential if the MIND recruitment pathway is crippled[64,66]. Ndc80c is a roughly 65 nm coiled coil with globular domains at either end[67,68]. At the inner kinetochore targeting end the c-terminal globular domains of Spc24 and Spc25 contain a RWD domain that allows for binding to MIND[69]. A coiled-coil emerges from these globular domains and connects to the c-terminal coiled-coil of Ndc80 and Nuf2 through a tetramerization domain, which involves overlapping contacts of all four proteins. The n-terminus of Ndc80 and Nuf2 form globular domains as well. Here Ndc80 and Nuf2 contain closely paired calponin homology domains (CH domain) by which the complex can bind directly to microtubules[70,71]. This occurs through interaction of positively charged residues of the CH domain and negatively charged tubulin c-terminal tails, inserting the CH domain into the interface between tubulin monomers in the microtubule[71,72]. Additional interactions with the microtubule can occur through a roughly 100 residue disordered n-terminal tail on Ndc80. Though this tail is nonessential, phosphorylation of several of its residues by the kinase Ipl1 can reduce the affinity of Ndc80c for the microtubule by the introduction of negative charges and consequent repulsion of the tail from the microtubule[73].

Spc105c (proteins Spc105 and Kre28) also interacts with the MIND complex via RWD domains at the Spc105 c-terminus through a separate site from Spc24 and Spc25, along the helical bundle[74-76]. The n-terminus of Spc105 consists of a disordered tail that contains over 400 residues. Within this disordered stretch are 6 MELT motifs, which can be phosphorylated by the conserved kinase Mps1[77]. This phosphorylation recruits the proteins Bub1 and Bub3, which can subsequently form the mitotic checkpoint complex[78]. The mitotic checkpoint complex can then trigger the spindle assembly checkpoint, pausing mitosis before anaphase. This process is critical for correcting erroneous attachments of kinetochores to microtubules that would otherwise result in missegregation events[79].

Like CCAN, MIND, Ndc80c, and Spc105c are structurally very well conserved across species. Work with the human homologs (Mis12, Ndc80c, Knl1c, together referred to as KMN) has provided informative structures of KMN[74,75]. In these structures the Mis12 complex binds Spc24/Spc25 sequentially, creating a fairly rigid ~30 nm rod of helices spanning the entirety of Mis12 and Spc24/Spc25 through the tetramerization domain (Nuf2 and Ndc80 were not present in these structures). The RWD domains of Knl1 and a small portion of Zwint (Kre28 in yeast) are also visible in this structure, binding alongside the rod of Mis12[74,75]. These structures nicely recapitulate previous work in both yeast and animals, and though Ndc80c was not present in these works, they present this key outer kinetochore complex as a series of nearly 100 nm rods which when oligomerized onto the inner kinetochore can reach out to encompass a spindle microtubule[59,61,74-76].

In yeast the heterodecameric Dam1c (proteins Ask1, Dad1, Dad2, Dad3, Dad4, Dam1, Duo1, Hsk3, Spc19, and Spc34) also engages the microtubule[80]. These 10 proteins come together to form a T-like structure which can then further oligomerize into a 17 member ring around the microtubule, with the top of the T near the lattice of the microtubule and the long stem at a shallow angle away from the lattice[81-83]. There is a 6 nm gap between the Dam1c ring and the microtubule, and it is thought that this along with the electrostatic nature of Dam1c-microtubule interaction contributes to the rings ability to diffuse along the microtubule[81,83]. Due to its low abundance in the cell it is expected that Dam1c can only form 1-2 rings per kinetochore, and in fact cryo-electron tomography (cryo-ET) studies in using serial cryosectioned yeast cells have reported that over half the Dam1c visible on spindle microtubules forms partial rings[84]. Dam1c rings interact with Ndc80c at 3 locations: near the CH domain through a flexible tail on Dam1, near the Ndc80 hinge through a flexible tail on Ask1, and near the tetramerization domain through the protrusion of Spc19 and Spc34[85]. Loss of Dam1c significantly impacts the ability of kinetochores to sustain binding to microtubules under tension[86].

Tension itself is a key to kinetochore function. Studies with purified kinetochore particles have shown that tension directly stabilizes kinetochore-microtubule attachment[86]. The resultant catch-bond mechanism is thanks to the conserved XMAP215 family protein Stu2 that binds near the tetramerization junction of Ndc80c[87,88]. This tension sensitivity offers an intrinsic error correction mechanism within the kinetochore. Bioriented kinetochores will experience tension through the pulling forces of microtubules from opposite spindle poles. By contrast, incorrectly attached sister kinetochores in which only one kinetochore is attached or both kinetochores are attached to microtubules from the same pole will not. Because tension stabilizes kinetochore microtubule interactions, correct attachments will be stabilized while incorrect ones will be turned over, allow the cell to try again[89,90]. Interestingly, applying tension to kinetochore particles bound to microtubules also seems to attenuate Ipl1 phosphorylation of the Ndc80 tail, which in turn stabilizes the binding of Ndc80 to the microtubule, providing evidence for a tension dependent conformational change based mechanism for stabilizing correct kinetochore-microtubule interactions that is distinct from Stu2[91].

1.4 Towards a complete model of kinetochore architecture

The previous chapters illustrate the myriad of components and functions of the kinetochore. Decades of research have provided an abundance of useful information; however the field still lacks a cohesive architectural model of the complete kinetochore. Though structures have provided tremendous insight into the organization of solid assemblies such as the nucleosome, Cbf3, CCAN, KMN, and the Dam1c ring, fitting those assemblies together has proved challenging. Contacts between Cse4 and Chl4 of the CCAN have been shown to be important biochemically, but don't seem to be recapitulated in the latest structures. Additionally, it is difficult to discern in these structures why contacts between Cse4 and Ame1 should be critical to kinetochore function. Structures of Cbf3 and CCAN are also difficult to reconcile, as it

is thought that Cbf3 remains at the kinetochore, yet its full structure and that of CCAN would face significant steric clashes if bound at the same time. The organization of the outer kinetochore complexes on the CCAN is also unclear and expected to be highly flexible due to the disordered nature of the connections between the inner and outer kinetochore. Even with the outer kinetochore, though the core KMN components and Dam1 ring structure is generally agreed upon, the field is still deciphering how these two assemblies interact in the context of microtubule binding. How additional proteins like Stu2 and Mps1 associate with Ndc80 in a way that lets them modulate kinetochore activity is also an active area of study. To understand how the kinetochore can achieve its function it is necessary to develop an architectural model that defines the spatial relationships between all of these assembled regions, and in order to do that it would be ideal to directly examine native and fairly complete kinetochore particles.

Previous attempts have been made to study purified native kinetochore particles[92]. Though this work offered exciting glimpses of microtubule binding globular domains organized around a central hub the kinetochore particles were lowly abundant and unstable on electron microscopy (EM) grids, significantly limiting the conclusions that could be drawn from this study. In the following chapters, I describe my work building on this original study by taking advantage of the thermotolerant yeast *Kluyveromyces marxianus* to purify more stable kinetochore complexes for EM. This work biophysically characterizes these kinetochores and provides significantly improved views, including by cryo-ET. We also reconstruct whole mitotic spindles and use this data to argue *K. marxianus* utilizes a point centromere despite the presence of linked kinetochores visible by EM.

Chapter 2: Architecture of native kinetochores revealed by structural studies utilizing a thermophilic yeast

At time of writing, the contents of this chapter are under review for publication with the following authors and corresponding contributions:

Authors: Daniel J. Barrero, Sithara S. Wijerante, Xiaowei Zhao, Grace F. Cunningham, Rui Yan, Christian R. Nelson, Yasuhiro Arimura, Hironori Funabiki, Charles L. Asbury, Zhiheng Yu, Radhika Subramanian, Sue Biggins.

Author contributions: Conceptualization: DJB and SB; Data Curation: DJB and XZ; Funding Acquisition: DJB, SB and HF; Investigation: DJB, SSW, and GFC; Methodology: DJB, SB, SSW, YA, XZ, RY, CRN, and ZY; Project Administration: SB and RS; Resources: DJB, SB, and ZY; Software: XZ, RY, and CLA; Supervision: SB, HF, and ZY; Validation: DJB; Visualization: DJB, SSW, GFC, XZ, and ZY; Writing – Original Draft: DJB and SB; Writing – Reviewing and Editing: DJB, SB, CLA, YA, HF, SSW, GFC, CRN, and RS.

2.1 Summary

Eukaryotic chromosome segregation requires kinetochores, multi-megadalton protein machines that assemble on the centromeres of chromosomes and mediate attachments to dynamic spindle microtubules. Kinetochores are built from numerous complexes, and understanding how they are arranged is key to understanding how kinetochores perform their multiple functions. However, an integrated understanding of kinetochore architecture has not yet been established. To address this, we purified functional, native kinetochores from *Kluyveromyces marxianus* and examined them by electron microscopy, cryo-electron

tomography and atomic force microscopy. The kinetochores are extremely large, flexible assemblies that exhibit features consistent with prior models. We assigned kinetochore polarity by visualizing their interactions with microtubules and locating the microtubule binder Ndc80c. This work shows that isolated kinetochores are more dynamic and complex than what might be anticipated based on the known structures of recombinant subassemblies and provides the foundation to study the global architecture and functions of kinetochores at a structural level.

2.2 Introduction

To accurately partition chromosomes during cell division, eukaryotic cells utilize kinetochores to harness the growth and shortening of spindle microtubules to carry chromosomes toward the spindle poles[35-37]. The kinetochore assembles at the centromere, a specialized region of the chromosome that is epigenetically specified by a centromeric histone variant called CENP-A (Cse4 in budding yeast)[38,93,94]. Multiple copies of kinetochore complexes called the constitutive centromere associated network (CCAN) assemble on centromeric chromatin to create the inner kinetochore[47,95-98]. The CCAN recruits additional outer kinetochore complexes that bind directly to spindle microtubules to complete the link between the chromosome and the force generating microtubule[70,83,99,100]. In addition to their fundamental role in microtubule attachment, kinetochores also serve as a dynamic signaling hub for mitosis, sensing tension and microtubule attachment as well as creating a scaffold for the spindle assembly checkpoint[77,86,87,101,102]. The mechanisms that underly these diverse kinetochore roles are still an open area of research and a critical step in understanding these functions is to elucidate the structure of the kinetochore.

Major challenges for structural studies of the kinetochore are the size, complexity, and dynamics of these machines. Mammalian centromeres span megabases of DNA and contain hundreds of kinetochore proteins that attach to multiple microtubules[37,95]. In contrast, budding yeasts have simple point centromeres that contain a single centromeric nucleosome and bind to

one microtubule[38,41,42,103]. Despite these differences, the major components and functions of kinetochores are conserved between yeast, mammals, and several other model systems. Approaches focused on specific kinetochore complexes have yielded structural information and insights into kinetochore complexes and larger assemblies in recent years[97,104]. Nearly complete yeast and human CCAN complexes, with some including the centromeric nucleosome, have been solved[50,54,105,106]. These structures demonstrate that the 14-member CCAN complex comes together to form a wishbone-like shape, creating a slot in which the centromeric nucleosome can anchor. However, the precise connections between CCAN and the nucleosome have not been visualized[107] (Fig. 1A).

Extensive structural work has also been done on outer kinetochore complexes. The MIND heterotetramer (Mis12 in humans) that links the microtubule binding complexes to the inner kinetochore assembles into a long Y-shaped structure, with all the N-termini of its components located in the two “heads” of the Y, and their C-termini located in the tail[59,60]. The yeast MIND head regions bind to the inner kinetochore yeast proteins Ame1 (CENP-U in humans) and Mif2 (CENP-C in humans)[59,60]. The C-termini in turn bind to the Ndc80 complex (Ndc80c), thus completing a continuous connection from the microtubule to the chromosome (Fig. 1A). The Ndc80c is a heterotetramer that comes together to form an extended coiled-coil with globular domains at both ends[68,108,109]. The globular domains comprised of Spc24 and Spc25 contact the C-terminus of the MIND complex, while the globular domains of Nuf2 and in particular Ndc80 contact the microtubule[72,99,100,110]. Ndc80c is also recruited by the inner kinetochore Cnn1 complex (Cnn1c; CENP-TW in humans) which competes with the MIND pathway in yeast[64,111,112] (Fig. 1A). How these two pathways are integrated in the kinetochore is an open area of study.

Despite the tremendous progress in solving structures of various kinetochore subregions, it has been difficult to build a cohesive, complete model of kinetochore architecture. The precise copy number of protein complexes, especially in the outer kinetochore, remains

unclear[113-116]. Furthermore, the links between the inner and outer kinetochore are made by proteins with long tails that are predicted to be disordered, reaching out to contact the outer kinetochore. Indeed, for many structures of kinetochore complexes it was necessary to remove or reduce flexible elements from the proteins, and in some cases only short regions of some component proteins remain visible in the structures. It is therefore unclear how the tails extend from the CCAN to the outer kinetochore. The available outer kinetochore substructures also lack many proteins that are required for sensing the attachment state of the kinetochore and serving as a signaling hub during mitosis, as well as post-translational modifications known to contribute to kinetochore assembly and function[59,66,101,117,118]. To address these concerns, we must understand the spatial relationships of these different regions in natively assembled kinetochores.

The only organism from which large native kinetochore assemblies have been isolated to date is the budding yeast *Saccharomyces cerevisiae*. In 2010, native kinetochore particles that could maintain microtubule attachments under physiological forces were purified from *S. cerevisiae*[86]. These kinetochore particles were used in negative stain electron microscopy experiments to provide novel views of isolated kinetochores, however the strong tendency for the kinetochores to aggregate and denature on the grids made it difficult to draw conclusions about the architecture[92]. Likewise, attempts to visualize kinetochores bound to microtubules in vitreous ice have offered exciting glimpses of cloud-like protein masses associated with kinetochore components but have not resulted in sufficient details to describe their architecture[119]. To overcome these limitations, we sought to purify native kinetochores from a thermophilic organism because their adaptation to live at high temperatures seems to facilitate structural biology[120-122].

Here, we report the purification of native kinetochores from the thermophilic yeast *Kluyveromyces marxianus* and show that they contain all known kinetochore proteins and are functional to bind to microtubules under force. These kinetochores are more amenable to

electron microscopy than those from *S. cerevisiae*, and we provide views of complete, native kinetochores in ice. We visualize these kinetochores bound to stabilized microtubules and identify the locations of microtubule binding complexes and the inner kinetochore within the architecture of these particles. We confirm the shape of these particles by real-time high-speed atomic force microscopy (HS-AFM) in liquid. These particles are dynamic and much larger than any previously visualized kinetochore assemblies. This work lays the foundation for understanding how individual kinetochore complexes fit into a unified kinetochore architecture, and how this architecture enables kinetochore functions.

2.3 Results

2.3.1 Functional native kinetochores can be purified from *K. marxianus*

We set out to purify kinetochores from a thermophilic yeast to determine whether they are more stable for structural studies than those of *S. cerevisiae.* We first determined whether *K. marxianus* had homologs of the 40 established *S. cerevisiae* kinetochore proteins by identifying previously assigned kinetochore proteins in the NCBI *K. marxianus* database (Taxon ID: 4911; Table 1, higher alignment scores and lower E. values indicate better matches). For the 10 proteins that were not previously assigned, we identified homologs in *K. marxianus* by either local alignment searches using *S. cerevisiae* proteins or *Kluyveromyces lactis* proteins (Table 1). We detected all expected kinetochore proteins except Iml3 (CENP-L in humans), which is nonessential for vegetative growth in budding yeast but essential for meiosis[52].

The strong similarity between the kinetochores in the two yeast species suggested that our previously described method to purify *S. cerevisiae* kinetochores via a one-step purification of the Dsn1 kinetochore protein might work in *K. marxianus*[16]. We therefore tagged the *K. marxianus DSN1* gene at the endogenous locus with 6xHis and 3xM3DK epitopes (Dsn1-His-M3DK). Cells were treated with benomyl, which suppresses microtubule dynamics, to enrich for

mitotic cells and to reduce cell cycle stage variability. Kinetochores were captured from lysates using a-M3DK beads and then eluted with M3DK peptide. The elutions produced consistent banding patterns as visualized on a silver-stained gel (Fig. 1B). We performed mass spectrometry to identify the co-purifying proteins and confirmed the presence of proteins from every kinetochore subcomplex except the nonessential Cnn1c (Fig. 1C, Table 1). Kinetochore complexes were significantly enriched compared to purifications from negative control strains lacking the M3DK tag on Dsn1 (Supplemental Fig. 1A). Outer kinetochore proteins tended to be slightly overrepresented in terms of peptide spectrum matches (PSMs), consistent with the observation that outer components are present at higher copy numbers[53]. To further confirm that specific kinetochore proteins co-purified with Dsn1, we generated antibodies to representative members of the Dsn1 complex (Nnf1), the outer kinetochore Ndc80 complex (Spc24), and the inner kinetochore CCAN (Okp1) and performed immunoblotting on the purified particles. We detected these components, demonstrating that the purified particles spanned the inner to outer kinetochore (Fig. 1D). Taken together, these data suggest that purifying Dsn1 leads to the isolation of relatively complete kinetochores from *K. marxianus*. To ensure that a stable kinetochore complex was purified, we loaded the kinetochore purifications onto a 20%-60% glycerol gradient and analyzed the fractions by immunoblotting with antibodies against various kinetochore proteins. The gradient separated unbound kinetochore complexes from a small pool of assembled kinetochores (Supplemental Fig. 1 B, C), demonstrating that there is a population of stable and relatively complete kinetochores.

To test whether the *K. marxianus* native kinetochores retained their key function of binding to microtubules under force, we used a previously established optical trapping assay that measures the strength of kinetochore-microtubule attachments[16]. Kinetochores were conjugated to polystyrene beads and these beads were introduced to microscope slide chambers with dynamic microtubules seeded on the coverslip surface. A single bead was trapped by a focused infrared laser and brought into proximity of a single microtubule tip to

create a kinetochore-microtubule interaction. The strength of the interaction was measured by applying tension until the bead detached from the microtubule (rupture event), the maximum strength of the trap was reached, or the measurement was otherwise interrupted (escape event). *K. marxianus* kinetochores exhibited robust microtubule attachments with a similar median rupture force to kinetochores purified from *S. cerevisiae* - median rupture forces of 7.5 pN and 7.2 pN, respectively. However, the distribution of events for *K. marxianus* appeared bimodal, with a high strength cluster that does not appear in *S. cerevisiae* (Fig. 1E). Despite the similarity of the median rupture forces, this difference in distribution is significant by a log-rank test (p value = 0.04) and its source is an area of future investigation. Together, these data show that *K. marxianus* kinetochores can maintain attachments at slightly higher forces than *S. cerevisiae* (Fig. 1E), confirming their functionality.

2.3.2 Two classes of kinetochores are visible by electron microscopy

We next performed negative stain electron microscopy as a first step toward elucidating kinetochore architecture. Purified kinetochores were deposited on electron microscopy grids, stained with uranyl formate, and then imaged. Kinetochores appeared as large paintbrush-like structures with a flared “brush” end and a more compact hub, which often had a long thin projection, akin to a paintbrush “handle” (Fig. 2). A population of these kinetochores appeared as doublets, with two brushes connected by their handles (Fig. 2B). The average proportion of doublets was higher than singlets (Fig. 2; 64% doublets, 36% singlets; SEM = 11%; n = 50 kinetochores). We occasionally saw singlet kinetochores without a “handle” projection, which may be due to degradation during sample preparation or may represent an intermediate between singlets and doublets.

A key to interpreting the architecture of the kinetochore particles was to establish the polarity of inner and outer kinetochore regions. The branched architecture visible by negative stain appeared consistent with the hierarchical structure proposed for the kinetochore, with

relatively few copies of inner kinetochore complexes building to many copies of outer kinetochore complexes[46,54]. We therefore hypothesized that the wider “brush” end (Fig. 2, blue arrows) consisted of the outer kinetochore microtubule binders and the more tapered regions contained the inner kinetochore DNA binding proteins (Fig. 2, orange arrows). The inner kinetochore could potentially contain the centromeric DNA which forms the nucleosome required for kinetochore assembly. If this were true, treatment with a nuclease might degrade the compact hub or the handle if DNA was present. To test this hypothesis, we performed a short, room temperature incubation with or without a high concentration of nuclease (benzonase) just prior to the last two washes. We then removed the benzonase with the final washes before the kinetochores from beads. Although the compact hub remained largely intact, the proportion of doublets decreased significantly from 36% to 21% ($p < 0.001$, Fig 2C). The clear shift from doublets to singlets with nuclease treatment suggests that there is exposed nucleic acid in the handle of the kinetochores, and that it is partially responsible for maintaining the doublet connection.

2.3.3 Kinetochores interact with microtubules through the brush tips

Our discovery that the handle is sensitive to nuclease treatment and is therefore proximal to the inner kinetochore suggested that the brush tips contained the outer kinetochore (Fig 2, blue arrows). To test this, we incubated purified kinetochores with taxol-stabilized microtubules and imaged them by negative stain EM. From these micrographs, we visualized clear interactions of the brush tips with the microtubules (Fig. 3A). In cases where only a single region of the kinetochore contacted a microtubule, the brush tips were the most common point of contact (Fig. 3B, 40% compared to 5.8% and 1.2% for the compact hub and handle, respectively). However, it was not possible to normalize this data to account for the differences in 3D surface area between the regions of the kinetochore because this data cannot be calculated from 2-D images. In more rare views, either the compact hub or the handle could

occasionally be seen exclusively contacting the microtubule (Fig. 3A, B). We also asked whether the kinetochores had a preference between binding to the microtubule lattice or the tip by quantifying the position of the kinetochore on the microtubules and found there were no significant trends (Fig. 3C, Supplemental Fig. 2). Despite clear contact between the kinetochores and the microtubules, we were not able to detect the presence of Dam1c rings that were visualized in *S. cerevisiae* EM experiments[47]. However, Dam1c components were present in the mass spectrometry data even though they did not oligomerize around the microtubules. Due to the dense clouds of proteins at the brush tips, it was also difficult to distinguish individual microtubule binding sites on the kinetochores. Regardless, these data suggest that the brush projections contain the outer kinetochore complexes and that the purified kinetochores can bind to both the sides and ends of the microtubule.

2.3.4 Ndc80 is located in the brush

We next sought to determine whether the major microtubule binder Ndc80c is in the brush region by gold labeling, as the brush was long enough to contain the MIND/Ndc80c rod (Fig. 4A). We engineered a strain with a 3xV5 C-terminal tag on Ndc80p (Ndc80-V5) and then purified kinetochores from strains with or without the epitope tagged Ndc80. To perform the labeling, we conjugated V5 antibody to 10 nanometer gold beads, incubated the beads with purified kinetochores and then subsequently applied them to grids for negative staining. Ndc80-V5 kinetochores showed higher levels of gold labeling than those lacking the V5 tag (Fig. 4B). We quantified the location of gold beads on visible kinetochores, and there was a significant enrichment of gold particles in the distal region of the brush tips (Fig 4D, region S1). This data suggests that Ndc80c is in the brush, however the low level of gold labeling prevented us from identifying its location more specifically.

The negative stain data showed fibrils connecting the brush tips and compact hub (Fig 4A, region S2). These fibrils appear relatively rigid with an average length of roughly 54nm.

When added to the average length of the bulky brush tip density, roughly 42nm, these two sections span nearly 100 nm (Fig. 4A, regions S1 and S2). The Ndc80c is expected to be roughly 60 nm long, and when bound to the MIND complex the two form a roughly 90nm rod[33,55-57]. The fibrils and brush tips are therefore consistent with the length and shape expected of MIND attached to Ndc80c. The significant density at the bush tips is likely due to partner proteins known to bind with or near Ndc80c, such as Dam1c, Stu2, the large, disordered tail of Spc105, and Mps1[57-62].

2.3.5 Atomic force microscopy reveals kinetochore dynamics

To confirm the architecture using a different method as well as to examine kinetochore dynamics, we employed atomic force microscopy (AFM). AFM can provide information on dynamics and flexibility within individual kinetochore molecules, which were suspected to contribute to the difficulties with sub-tomogram averaging. Kinetochore particles were deposited on a mica surface and imaged. We first examined the surface topography of the individual kinetochore particles by imaging at a relatively slow scan rate (~5 Hz). We classified the observed structures into three categories by visual examination. The first category included particles with extended architecture. Consistent with the negative stain images, we observed a paintbrush-like architecture with a long handle extending from a brush head (Fig. 5A-C, 50% (n=68)). The second category consisted of more compact particles where the handle appears to be close to the brush head (Fig. 5D, E; 21% (n=29)). The third category had particles where the handle was not visible (Fig. 5F, G; 29% (n=40)). In addition, we occasionally observed doublets similar to those observed by tomography (Supplemental Fig. 3). The different extended and closed structures observed by AFM could arise from differences in the orientation of the particles on the mica surface. Alternatively, they may represent inherent dynamics and flexibility of the kinetochore. To distinguish between these possibilities, we performed high-speed AFM (HS-AFM) by imaging the same sample at a higher scan rate (100 Hz) to better visualize the

dynamics of the particles. The time-lapse data revealed conformational dynamics in the kinetochore particles, with significant changes in the observed extension of the handle regions over time (Fig. 5H; Supplemental movies 1,2). This is consistent with extended and compacted states observed by low-speed AFM imaging (Fig. 5A-G) and with the flexibility seen in negative stain EM. Dynamics were also observed in the brush head segment (Fig. 5H, Supplemental movies 1,2), which also likely contributed to the conformational heterogeneity observed.

2.3.6 Kinetochores are visible by cryo-electron tomography

Given the success in visualizing the kinetochores via negative stain, we sought higher resolution information. However, although the *K. marxianus* kinetochores were more abundant on grids than previous attempts with *S. cerevisiae*[47], it was still rare to image a negative stain grid with more than 100 total identifiable kinetochores. Due to the extremely low number of visible particles on grids, single particle cryo-electron microscopy was not an option. We therefore turned to cryo-electron tomography (cryo-ET) to maximize the information attained from each particle imaged. To increase the kinetochore concentration on grids, we employed magnetic isolation and concentration-cryo-electron microscopy (MagIC-cryo-EM) which uses magnetic nanobeads to capture and pull kinetochores to the grid surface using a strong magnet[63]. For unknown reasons, the kinetochores did not bind well to the magnetic nanobeads. However, the presence of the nanobeads improved the quality of the ice, leading to more visible kinetochores. We were able to collect over 100 tomograms of kinetochores that maintained the key features visible by negative stain, and occasionally showed an additional layer of density distal to the bulk of the brush tips (Fig. 6A, B, Supplemental Fig. 4, Supplemental movies 3,4). Although we made repeated attempts at sub-tomogram averaging using various strategies, they did not provide sufficient EM density maps to build structural models. This is likely due to kinetochore flexibility and heterogeneity combined with difficulty in maintaining the structural

integrity of the kinetochore in thin ice and a strongly preferred orientation which limited the potential views of the particles. Despite the inability to perform averaging, these tomograms provided improved views of several regions of the kinetochore (Fig. 6A, B). The linkages between the brush tips and the compact region appear as long and relatively rigid fibrils that are easier to distinguish compared to the negative stain images. They have a consistent length of about 35 nm. When the fibril length is added to the length of the bulky brush tip density (45nm), the combined length is ~80nm. This is slightly smaller than the ~100nm measured for this region by negative stain but is still consistent with a roughly 90nm rod like MIND/Ndc80c complex. The additional length in negative stain may be due to the stain flattening the proteins. The handle also showed more features than were visible in negative stain, revealing fibrous strands running parallel to the length of the handle. Occasionally a gap or donut-like structure appeared at the center of the handle (Fig. 6A, red arrow). The cryoET images also made it apparent that the handle does not protrude exactly from the center of the compact region, but rather from the outside edge. Quantifying the sizes of these kinetochores confirmed that they are highly flexible, apparent from the spread of measured distances, particularly along the transverse axes of the brush tips and fibrils (Fig. 6C, regions S1 and S2). They are also larger than those previously measured from *S. cerevisiae* with an axial length of roughly 243 nm (Fig. 6C, D)[40,47]. Interestingly, omitting the handle from these measurements brings the average axial length to roughly 131 nm, close to that reported in *S. cerevisiae*[40,47]. Together, these data are consistent with the predicted size and shape of kinetochores based on previous structural work and suggest a general conservation of kinetochore structure.

2.4 Discussion

Here we report the purification of native kinetochore particles from the thermophile *K. marxianus* that exhibit a high degree of completeness and retain their key microtubule binding ability. Though we did not detect Cnn1c in our purifications, this complex has been difficult to

detect by mass spectrometry in *S. cerevisiae* kinetochore purifications as well, and we lacked an appropriate antibody to probe for it by immunoblot. It is therefore unclear whether Cnn1c is present in the *K. marxianus* purifications. The *K. marxianus* particles were more stable than those purified from *S. cerevisiae*, allowing us to collect views of kinetochore particles by cryo-ET and AFM. The kinetochores had a paintbrush-like overall architecture, with many brush tips tapering into a compact hub and handle-like structure (Fig. 7). In addition, the brush tips and handle were flexible when analyzed by AFM. Using microtubule binding assays, we determined that the outer kinetochore region resides in the brushes, which have a size and shape consistent with Ndc80c and its associated proteins. We also identified nucleic acid within the handle through nuclease treatment, confirming it as adjacent to the inner kinetochore. This established inner/outer polarity within these kinetochore images and suggested the flexibility of the handle may be due to possible chromatin content.

One striking feature of the *K. marxianus* kinetochores is their size. The average axial length of a minimum kinetochore unit is ~131 nm, omitting the handle as kinetochores were occasionally seen without it. The average axial length of the handle alone is 112 nm, significantly increasing the overall size. However, the significant variability in the handle measurements and the dynamics seen by AFM suggest that the handle is very flexible and capable of undergoing compaction. Although the length of the *K. marxianus* kinetochore without the handle is close to isolated *S. cerevisiae* kinetochores (126 nm)[47], the EM measurements are larger than those attained by in vivo fluorescence work in *S. cerevisiae* that described a roughly 70 nm metaphase kinetochore and a 50 nm kinetochore in anaphase[40]. Some of this discrepancy may be due to EM methods. For example, negative staining can flatten complex protein assemblies, leading to some distortion or elongation[64], and the kinetochore may be particularly susceptible to this due to its highly flexible architecture. For cryoET sample preparation, the blotting procedure and the resultant thin solution layer before freezing may compress the kinetochore, causing it to spread out. Consistent with this, the kinetochore axial

distance measurements taken by AFM tended to show a more compact structure. Despite the size differences between the kinetochore particles and in vivo measurements from *S. cerevisiae* kinetochores, the MIND/Ndc80c proteins appear to form a 90nm rod like structure which is consistent with both the shape and length of what we propose the outer kinetochore is in these particles. In the future, resolving these questions will require generating sufficient electron density maps to build atomic models of the kinetochore subcomplexes within the structure.

The native kinetochores we visualized exhibit a more complicated architecture than previously published structures. The average axial and transverse lengths of the compact hub are roughly 52 nm and 90 nm, respectively. This is large enough to easily contain the largest published assembly of the yeast inner kinetochore, containing two CCANs, the centromeric nucleosome and a core Cbf3 complex[65]. However, the high flexibility and density of proteins within the kinetochores made it impossible to assign proteins or identify a CCAN-like structure. There are several possible reasons for this difficulty. First, native kinetochores likely retain much more protein than recombinant subcomplexes that lack parts of individual proteins. Second, compaction of the chromatin surrounding the centromeric nucleosome could also create a dense environment that obscures the CCAN. Consistent with this, chromatin has been shown to tightly compact in vitro at magnesium chloride concentrations similar to those present in the purification buffer[66]. We were also unable to discern the KMN network in the tomograms. However, additional large, flexible proteins bind to various members of the KMN[56,57,59,60]. Many of these proteins are present in the mass spectrometry data, including Stu2 and the Dam1 complex, and they could be responsible for much of the density seen at the brush tips (Fig. 7).

Another feature of kinetochores we identified is high flexibility of the connections between the inner and outer kinetochore. In yeast, the critical links between the inner and outer kinetochore occur through the essential proteins Ame1 and Mif2[30,31,54,67,68]. The connection between these proteins and the outer kinetochore occurs at the ends of domains which are predicted to be unstructured (Fig. 7, Supplemental Fig. 5). This is apparent in the cryo-ET

through the wide variety of configurations in which the kinetochores are seen, but particularly in the spread of the transverse length measurements for the outer kinetochore (Fig. 5C, region S1) and the axial length measurements of the handle (Fig. 6C, region S4). Dynamics in both regions were directly observed by high-speed AFM. The flexibility of the outer kinetochore may allow the microtubule binding elements to spread, increasing the effective surface area that can contact the microtubule and facilitating capture. The flexibility may also assist the kinetochore in maintaining contact with the microtubule in sub-optimal orientations. Consistent with this, kinetochores were seen in a range of orientations while interacting with microtubules. The ability to remain attached in many orientations may increase the robustness of the kinetochore-microtubule interaction, consistent with the ability of *K. marxianus* kinetochores to maintain attachment to microtubules at higher forces. The handle also appears to extend as seen by AFM. As the handle is expected to be in contact with DNA due to its position near the inner kinetochore, a potential explanation for this extension could be the unraveling of chromatin. Further exploration as to the nature and composition of the handle will be needed to better understand these dynamics.

An unexpected finding from this work was the presence of doublet and singlet kinetochores. Because nuclease treatment reduces the proportion of doublets and singlet kinetochores can occasionally be seen without visible handles, we propose that the functional kinetochore unit contains the brush tips to the compact hub and the handle links kinetochore units through their inner regions via nucleic acid. The average sizes of the individual kinetochore units within doublets are consistent with the average size of singlet kinetochores, but they are not identical in size. Furthermore, both kinetochore units in doublets can independently interact with microtubules, suggesting each is functional. The handle connecting doublets also shows interesting features. Its width is remarkably consistent when compared to the widths of the rest of the kinetochore and its dimensions are not far from what might be expected from a 30 nm chromatin fiber that forms in vitro at salt concentrations similar to our buffers[66]. In some cases,

the handles also show a ring-like gap, potentially indicating some kind of linkage or hinge point. We have three hypotheses for the functional role of doublets. First, *K. marxianus* may have small regional centromeres that bind to multiple microtubules and a doublet would bind to two microtubules. Another possibility is that each doublet binds to one microtubule. While *K. marxianus* and *S. cerevisiae* centromeres both contain three centromere defining elements (CDEI, CDEII, CDEIII), the length of CDEII in *K. marxianus* is nearly double that of *S. cerevisiae*[69] and may represent an important feature for building doublet kinetochores. A third possibility is that the doublets are sister kinetochores that were not broken apart during the purification process. However, proteins that link sister kinetochores such as cohesion were not readily detectable in our mass spectrometry data. Distinguishing these ideas will require determining the number of microtubule binding sites per centromere in vivo.

In the work presented here, we utilized a thermophilic yeast with conserved kinetochore proteins to purify native kinetochores that were amenable to structural biology. These kinetochores bear a striking similarity to the tri-laminar structure reported in the earliest EM images of mammalian kinetochores[70-72], with the inner plaque, translucent layer, and outer plaque mirroring the central hub, fibrils, and brush tips, respectively. The images also highlight the size and complexity of the kinetochore as it exists in its native environment and demonstrate that recombinant subassemblies are much simpler than the native structures. We were able to capture clear views of kinetochore interactions with microtubules, which will serve as the basis for understanding how many subcomplexes engage the microtubule tip, the details of how they do so, and how this process is regulated. Together, this work serves as the foundation for understanding the architecture of complete kinetochores, and how that architecture allows for its essential functions.

2.5 Materials and Methods

Strain construction

The *Saccharomyces cerevisiae* strain used in this study is SBY8253 (*DSN1-6xHis-3xM3DK:URA3*) and was derived from the W303 background and was previously described[86]. The *Kluyveromyces marxianus* strains used in this study are SBY18150 (*DSN1-6xHis-3xM3DK:KanMX*) and SBY21752 (*NDC80-6xHis-3xV5:NatMX*, *DSN1-6xHis-3xM3DK:KanMX*) and were derived from SBY17411 (NRRL Y-8281, USDA ARS culture collection). All strains were tagged at the endogenous locus. Briefly, DNA fragments of either 500 or 1000 bases immediately upstream and downstream of the desired integration site were generated from genomic DNA. A backbone plasmid was selected based on the desired tags, and the fragments amplified from genomic DNA were inserted into the backbone plasmid via Gibson assembly such that each plasmid contained a restriction site, followed by 500 to 1000 base pairs of upstream homology, followed by the desired tags and markers, followed by 500 to 1000 base pairs of downstream homology, followed by another restriction site. Plasmids were then digested and transformed into the desired strain for integration by homologous recombination. Successful integration was confirmed by PCR and immunoblotting. The plasmids (pSB prefix) and yeast strains (SBY prefix) used are as follows: SBY18150 contains plasmid pSB2951 generated with primers SB5736, SB5737, SB5738, SB5739, transformed into SBY17411; SBY21752 contains plasmid pSB3420 generated with primers SB7818, SB7819, SB7820, SB7821, SB7822, SB7823, transformed into SBY18150. All tagged strains grow similarly to the parent strain.

Yeast growth and kinetochore purification

All yeast growth was performed as described previously[86]. Briefly, yeast were grown in YPD (1% yeast extract, 2% peptone, 2% D-glucose). SBY18150 cultures were grown in the presence of 200 µg/ml G418. SBY21752 cultures were seeded from colonies grown on plates containing 100 µg/ml Nourseothricin Sulfate and were grown in the presence of 200 µg/ml G418 in liquid cultures as selection markers. Large cultures were grown on shakers (220 rpm) at 22

°C or 30 °C for *S. cerevisiae* and *K. marxianus,* respectively. Cultures were treated with benomyl at a final concentration of 30 µg/ml (1:1 addition of 60 µg/ml benomyl YEP media) for 2 hours at 23 ˚C and then harvested by centrifugation for 10 minutes at 5000xg at 4 ˚C. Kinetochores were purified as previously described[86]. Briefly, the endogenous *DSN1* kinetochore gene was C-terminally tagged with 6xHis and 3xM3DK. Harvested yeast were resuspended in Buffer H (25 mM HEPES pH 8.0, 150 mM KCl, 2 mM MgCl2, 0.1 mM EDTA pH 8.0, 0.1% NP-40, 15% glycerol) supplemented with protease inhibitors, phosphatase inhibitors, and 2 mM DTT. After resuspension and re-spinning, yeast pellets were frozen in liquid nitrogen and lysed using a Freezer Mill (SPEX, Metuchen NJ). Lysate was clarified via ultracentrifugation at 24,000 RPM (98,000 x g) for 90 minutes and the protein layer was extracted with a syringe. This extract was incubated with magnetic a-M3DK antibody conjugated Dynabeads (Invirtrogen, Waltham MA) for 90 minutes at 4 °C with rotation. For optical trapping, immunoblotting, and mass spectrometry, the Dynabeads were washed with 10x bead volume of Buffer H 5 times (the last 3 washes omitting DTT and phosphatase inhibitors). For optical trapping and immunoblots, kinetochores were eluted with 0.5 mg/ml 3xM3DK peptide in Buffer H lacking DTT and phosphatase inhibitors. For mass spectrometry, kinetochores were eluted from Dynabeads with 0.2% RapiGest (Waters Corporation, Milford MA) in 50 mM HEPES pH 8.0. For negative stain electron microscopy and cryo-electron tomography, kinetochores were washed with 10x bead volume of Buffer H 4 times (the last 2 washes omitting DTT and phosphatase inhibitors), followed by one wash in Buffer H-EM (25 mM HEPES pH 8.0, 150 mM KCl, 2 mM MgCl2, 0.1 mM EDTA pH 8.0) and elution with 0.5 mg/ml 3xM3DK (Genscript, Piscataway NJ) peptide in 1/3 the total volume of Dynabeads for negative stain experiments and ½ the bead volume for tomography. For all experiments, the total protein concentration was determined by NanoDrop measurement and purity by silver stain gel analysis.

Immunoblot and silver stain analyses

For immunoblot analysis, cell lysates were prepared as described above. Protein samples were separated using pre-cast 4-12% Bis Tris Protein Gels (Thermo-Fisher Scientific, Waltham MA) for sodium dodecyl sulfate-polyacrylamide gel electrophoresis (SDS-PAGE) in MOPS buffer pH 7.0 (20 mM MOPS, 5 mM sodium acetate, 1 mM EDTA). For immunoblotting, a 0.45 µm nitrocellulose membrane (BioRad, Hercules CA) was used to transfer proteins from polyacrylamide gels. The antibodies used for immunoblotting against Spc24, Nnf1 and Okp1 were custom generated by Genscript (Piscataway, NJ) against recombinant proteins that were expressed and purified from *Escherichia coli* and then injected into rabbits (Okp1: residues 190-440; Nnf1: full length protein; Spc24: full length protein). Genscript affinity purified the antibodies using the recombinant proteins and the resulting antibodies were used at the following dilutions: a-Spc24 used at 1:5,000; a-Nnf1 used at 1:2000; a-Okp1 used at 1:2000. Genscript services were also used to generate a m3DK nanobody (heavy chain variable region sequence: QVQLQQSAAELARPGASVKMSCKASGYSFTTYTIHWVKQRPGQG LEWIGYINPSSGYAAYNQNFKDETTLTADPSSSTAYMELNSLTSEDSAVYYCAREKFYGYDYW GQGATLTVSS; mouse IgG2a) which was used at 1:10,000. The secondary antibodies used were a sheep α-mouse antibody conjugated to horseradish peroxidase (HRP) (GE Life sciences, Marlborough MA) at a 1:10,000 dilution or a donkey α-rabbit antibody conjugated to HRP (GE Life sciences, Marlborough MA) at a 1:10,000 dilution. Antibodies were detected using the Super Signal West Dura Chemiluminescent Substrate (Thermo-Fisher Scientific, Waltham MA). For analysis by silver stain, the gels were stained with Silver Quest Staining Kit according to manufacturer's instructions (Invitrogen, Waltham MA).

Homology searches

To identify potential homologs of *S. cerevisiae* proteins in *K. marxianus* we performed a homology search. We used the *S. cerevisiae* kinetochore protein sequences available for the W303 background in the Saccharomyces Genome Database (SGD, Stanford University) and

searched against known *K. marxianus* proteins (NCBI TaxonID:4911) using the Basic Local Alignment Search Tool for proteins (BLASTp, National Institutes of Health). In cases where no homolog was found by this method, protein sequences from *Kluyveromyces lactis* were used in place of *S. cerevisiae.*

Optical trapping

Optical trapping rupture force assays were performed as previously described[86]. Streptavidin coated 440 nm polystyrene beads (Spherotech, Lake Forest IL) were functionalized with biotinylated a-penta-His antibody (Qiagen, Hilden Germany or R&D Systems, Minneapolis MN) and stored in BRB80 containing 8 mg/ml BSA and 1 mM DTT at 4 °C with continuous rotation. Beads were decorated with purified kinetochores (via Dsn1-6His-3M3DK) in a total volume of 20 µl incubation buffer (BRB80 containing 1.5 mg/mL κ-casein). To ensure sparse decoration of the beads and reduce the likelihood of multiple kinetochore-microtubule interactions being measured simultaneously, we empirically determined kinetochore concentrations such that roughly 1 in 10 beads exhibited microtubule binding activity during the assay. Dynamic microtubule extensions were grown from coverslip-anchored GMPCPP-stabilized microtubule seeds in a microtubule growth buffer consisting of BRB80, 1 mM GTP, 250 µg/ml glucose oxidase, 25 mM glucose, 30 µg/mL catalase, 1 mM DTT, 1.4-1.5 mg/mL purified bovine brain tubulin and 1 mg/mL κ-casein. Assays were performed at 23 °C. Rupture force experiments were performed as in[86]. Briefly, an optical trap was used to apply a force of ~1-2 pN in the direction of microtubule assembly. Once beads were observed to track with microtubule growth for roughly 30 seconds (to ensure end-on attachment), the applied force was increased at a constant rate of 0.25 pN/s until bead detachment. Records of bead position over time were generated and analyzed using custom software (LabVIEW and Igor Pro, respectively) and used to determine the rupture force, which was marked as the maximum force sustained by the attachment during each event.

Negative stain electron microscopy

3-5 µl of purified kinetochores were taken directly from elutions and deposited on glow discharged (Pelco easiGlow, Ted Pella, Redding CA) 400 mesh electron microscopy grids (01754-F F/C, Ted Pella, Redding CA) for 1 minute. Grids were then washed twice with water and once with 0.75% uranyl formate before staining for 45 seconds with 0.75% uranyl formate and drying overnight. Grids were imaged using a Talos L120C 120kV transmission electron microscope with a 4k x 4k Ceta 16m CMOS camera (ThermoFisher Scientific, Waltham MA) at a magnification of 36,000x and a pixel size of 4.11 angstroms at a nominal defocus of 2 µm under focus.

Microtubule binding experiments

For microtubule binding experiments, microtubules were prepared as follows: purified bovine tubulin was incubated at a concentration of 2 µg/µl in BRB80 with 6 mM magnesium chloride, 1 mM GTP, and 3.8% DMSO. The tubulin was allowed to polymerize for 30 minutes at 37˚C and then 0.01 mM paclitaxel in BRB80 was added at a volume equal to half that of the polymerization mixture (i.e. 100 µl for 200 µl of mixture) and mixed with wide bore pipette tips. The resulting mixture was then spun at 58,000 rpm for 10 minutes at 37 ˚C and the supernatant discarded. The pellet was resuspended with 0.01 mM paclitaxel in BRB80 at a volume equal to that of the original polymerization mixture. These microtubules were mixed 1:20 in eluted kinetochores and incubated for ~15 minutes at room temperature before applying to grids for negative staining.

Gold labeling experiments

a-V5 antibody was conjugated to 10 nm gold particles (Abcam, Cambridge UK) following the product recommended protocol. Kinetochores were purified as specified above for negative

stain. Antibody conjugated gold particles were incubated with kinetochores at a ratio of 1:100 for 30 minutes at room temperature with rotation. This mixture was used to prepare grids as described above and imaged with the same parameters. Gold labeling was quantified by hand, and a gold particle was determined to be in contact with a kinetochore if it was overlapping or within 10 nm of visible kinetochore density.

Nuclease digestion experiments

Dynabeads were used to bind kinetochores from yeast lysate as described above. To keep the kinetochore concentration consistent across replicates, the lysate was diluted such that 50 µl of beads were used for every purification. Kinetochore-decorated beads were washed with 1 ml of Buffer H 6 times (the last 3 washes omitting DTT and phosphatase inhibitors). While on beads, the kinetochores were incubated with or without 500 units of benzonase (Millipore Sigma, Burlington MA) per milliliter of reaction volume. This mixture was rotated at room temperature for 15 minutes before washing the beads twice with buffer H-EM and elution in ½ the bead volume with 0.5 mg/ml M3DK peptide. Grids were prepared as described above. Quantification of the proportion of doublets was performed by hand.

CryoEM grid preparation

Kinetochore purification was performed as described above. Purified kinetochores were incubated with biotinylated a-His antibody (R&D Systems, Minneapolis MN) at an antibody concentration of 0.025 ng/µl for 1 hour at 4 ˚C with rotation. Samples were then mildly crosslinked using a final concentration of 0.01% glutaraldehyde for 15 minutes on ice and quenched with a final concentration of 50 mM tris pH 7.4 buffer for 15 minutes. The crosslinked kinetochore/antibody sample was incubated with 50 nm magnetic nanobeads (CD Bioparticles, Shirley NY) which had been conjugated to a 60 nm single a-helix spacer protein terminating in a SPY-tag, which had in turn been conjugated to a SPY catcher/avidin. The nanobeads were

incubated with the kinetochores at a final concentration of 1 ug/ml. This mixture was incubated for 90 minutes at 4 ˚C, at which point it was spun at 12,000xg for 15 minutes at 4 ˚C to pellet. To minimize the loss of kinetochores that may not have been attached to beads, 2/3 of the supernatant volume was removed and the remaining 1/3 was used to resuspend the pelleted beads (as opposed to removing all the supernatant and resuspending in fresh buffer). The resuspended nanobeads were sonicated for 10 minutes in a water bath sonicator (Emerson, St. Louis MO) at 4 ˚C. 2.5 µl of sample was applied to 300 mesh Quantifoil R 2/1 copper grids (Electron Microscopy Sciences, Hatfield PA) that had been previously glow discharged (15 mA, 30 seconds; PELCO easiGlow, CA). Sample was incubated for 30 seconds at room temperature before manually wicking with a filter paper and re-applying. The grid was then held over a strong magnet for 30 seconds before being placed into a Vitribot Mark IV and blotted with the following settings: blot time:3; blot force: 7; wait time: 0; temperature: 22˚C; humidity: 100%. 2 filter papers were additionally used per blotting surface in the Virtibot.

Cryo-electron tomography data collection and image processing

Frozen kinetochore samples were imaged on a 300 kV Titan Krios (ThermoFisher Scientific, MA) equipped with a high-brightness Field Emission Gun (x-FEG), a spherical aberration corrector, a GIF Bioquantum energy filter and a K3 direct electron detector (Gatan, Inc., CA). The spherical aberration coefficient of the objective lens on the microscope was reduced from an uncorrected 2.7mm to ~0.01mm. The K3 camera was operated in counted mode with a binning of 0.5 with dose fractionation enabled. Tilt series were collected using SerialEM[134] dose-symmetric scheme with a tilt range of +/- 60°, a tilt step of 3°, and grouping of three images on either side (0°, 3°, 6°, 9°, -3°, -6°, -9° …). At each tilt, movies of 8 frames were acquired on the K3 camera. Data was acquired at two different magnifications with calibrated pixel size corresponding to 2.02 Å and 1.32 Å respectively. The total dose applied to each tilt series was 120 $e^-/Å^2$ and the nominal defocus was set to -2.5 µm for each tilt after autofocusing

on nearby area. Motion correction was performed for each movie in Relion[135] to reduce motion-induced blurring effect. Motion-corrected micrographs were combined to form tilt series with the proper angular order using home-written script. Then the tilt series were automatically aligned by IMOD batchruntomo and reconstructed by tomo3d[136,137]. The final tomogram reconstructions were post-processed by IsoNet to denoise and compensate missing wedge effect[138].

Atomic force microscopy

Kinetochore samples were diluted in BRB80 (80 mM PIPES pH 6.8, I mM EGTA) buffer supplemented with 5 mM $MgCl_2$ to concentrations varying between 30 and 80 mg/mL. Concentrations were optimized to create imaging fields with single, well-spaced kinetochores. For static imaging, approximately 20 µL of BRB80 + 5 mM $MgCl_2$ buffer and 20 µL of kinetochore sample were deposited on a freshly cleaved mica surface and allowed to incubate for ~10 minutes. After incubation, 20 µL of buffer was added to a tip, and additional buffer was added to the mica surface accordingly to maintain a proper volume of liquid for imaging. To locate kinetochores of interest, a scan area of 4 x 4 μm^2 was imaged. Areas that appeared to contain adequately spaced, single kinetochores, were then imaged using a scan area of 500 x 500 nm^2 to further resolve kinetochore structure. For high-speed imaging, the following process was repeated, with volumes of 10 µL, rather than 20 µL.

All imaging was performed on the Asylum Cypher VRS AFM using tapping mode in liquid. Static images were acquired with a silicon BL-AC40TS tip (radius: 8 nm, resonance frequency: 110 kHz, spring constant: 0.09 N/m; Oxford Instruments, Abingdon UK). Before imaging, set point, scan lines, and scan rate were set to 500 mV, 256 ´ 256 pixels, and ~1.5 Hz, respectively. In liquid, the drive frequency of the tip was ~20 kHz. For high-speed imaging, a silicon USC-F1.2-k0.15-10 tip (radius: <10 nm, resonance frequency: 1.2 MHz, spring constant: 0.15 N/m, NanoAndMore, Watsonville CA) was used. Set point, scan lines, and scan rate were set to 250 mV, 256 x 256 pixels, and ~10 Hz, respectively. In liquid, the drive frequency of the tip

varied between 450 and 550 kHz. Throughout both static and high-speed imaging, drive amplitude was maintained slightly above the point at which the tip started to contact the surface. Raw AFM data were processed using the Asylum Research (version 16.14.216) software. Static images, as well as images isolated from dynamic videos, were flattened using the magic mask feature. Height profiles were then created on the AFM height images.

Structural predictions

K. marxianus homologs were found by local sequence alignment searches as described above. ColabFold[139] was used to predict the structure of proteins which form a link between the inner and outer kinetochore (Cnn1, Ame1, Mif2). The full length of the *K. marxianus* proteins were used for structural predictions.

Statistical analysis, and figure generation

Statistical analysis was carried out with a variety of Python packages including: Lifelines for generation of rupture force survival curves and log-rank tests; Pandas for descriptive statistics of negative stain and cryo-ET measurement, microtubule binding, and gold labeling data. Optical trapping survival curves were generated in Python with Lifelines. Graphs for the proportion of doublets and singlets in negative stain, kinetochore microtubule interactions, and gold labeling were generated in python using Seaborn. Tomography distance boxplots were created in Python using Matplotlib. Scatter plots were generated in R with ggplot2. Gel images were cropped in Adobe Illustrator (Adobe, San Jose CA). Figures of protein structural models and alignments were generated in Chimera (University of California, San Francisco). Kinetochore cartoons were generated in Adobe Illustrator (Adobe, San Jose CA).

2.6 Figures & legends

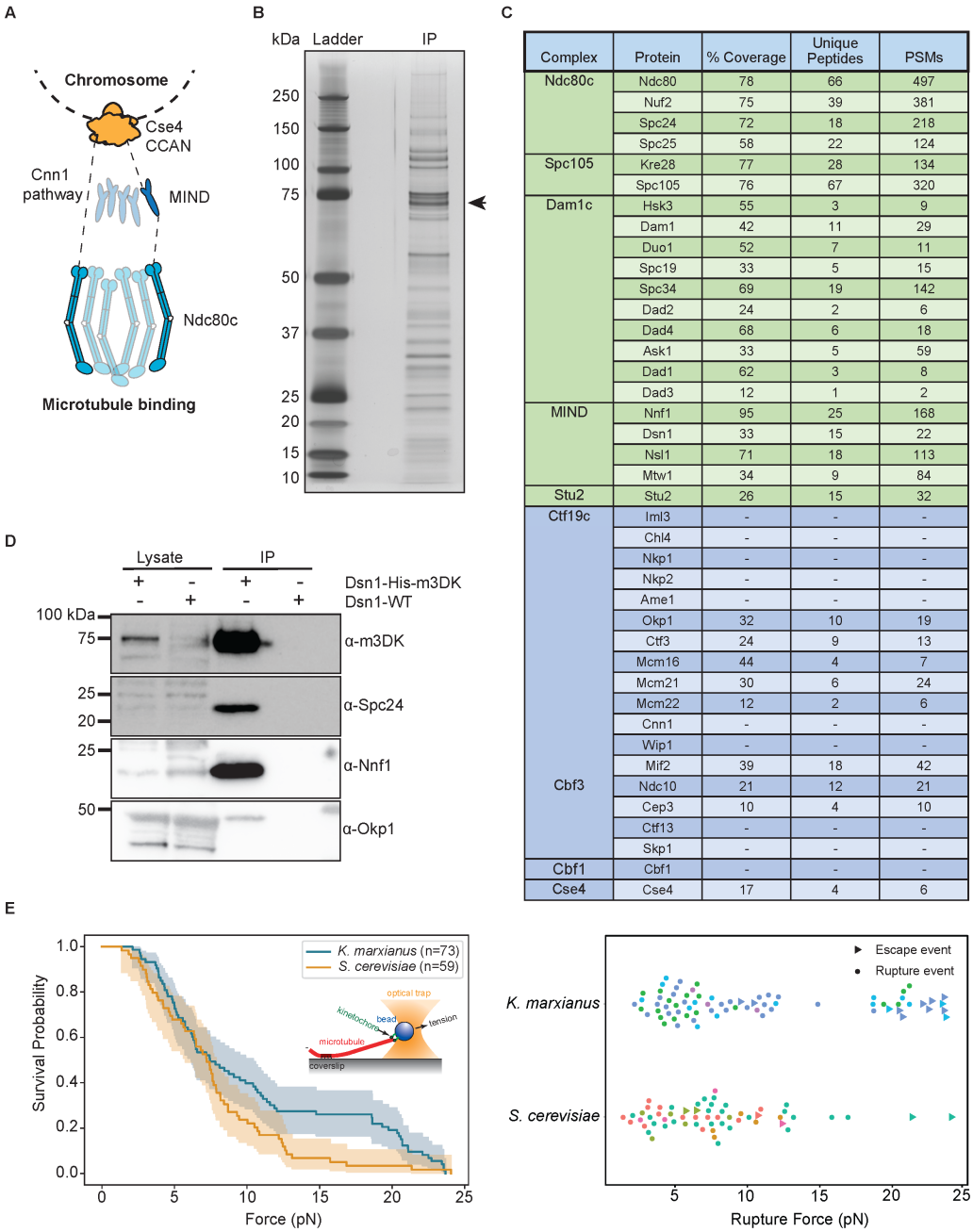

C

Complex	Protein	% Coverage	Unique Peptides	PSMs
Ndc80c	Ndc80	78	66	497
	Nuf2	75	39	381
	Spc24	72	18	218
	Spc25	58	22	124
Spc105	Kre28	77	28	134
	Spc105	76	67	320
Dam1c	Hsk3	55	3	9
	Dam1	42	11	29
	Duo1	52	7	11
	Spc19	33	5	15
	Spc34	69	19	142
	Dad2	24	2	6
	Dad4	68	6	18
	Ask1	33	5	59
	Dad1	62	3	8
	Dad3	12	1	2
MIND	Nnf1	95	25	168
	Dsn1	33	15	22
	Nsl1	71	18	113
	Mtw1	34	9	84
Stu2	Stu2	26	15	32
Ctf19c	Iml3	-	-	-
	Chl4	-	-	-
	Nkp1	-	-	-
	Nkp2	-	-	-
	Ame1	-	-	-
	Okp1	32	10	19
	Ctf3	24	9	13
	Mcm16	44	4	7
	Mcm21	30	6	24
	Mcm22	12	2	6
	Cnn1	-	-	-
	Wip1	-	-	-
	Mif2	39	18	42
Cbf3	Ndc10	21	12	21
	Cep3	10	4	10
	Ctf13	-	-	-
	Skp1	-	-	-
Cbf1	Cbf1	-	-	-
Cse4	Cse4	17	4	6

Figure 1. Functional kinetochores can be purified from *K. marxianus*. A) A schematic of kinetochore organization in *S. cerevisiae*. Ndc80c is recruited by either Cnn1 (left) or the MIND complex (right). B) Kinetochores purified via Dsn1-6His-3M3DK (from strain SBY18150) visualized by silver stain. The arrow indicates the position of Dsn1-m3DK which is inferred from

immunoblotting. C) A table of kinetochore proteins from a representative mass spectrometry experiment of purified *K. marxianus* kinetochores. Rows colored green are outer kinetochore proteins and rows colored blue are inner kinetochore proteins. Proteins not found in the mass spectrometry data are indicated by dashes. PSM refers to peptide-spectrum matches. D) Immunoblotting of representative components of the inner and outer kinetochore with the indicated antibodies. Lysate samples were collected before kinetochore purification. Immunoprecipitation (IP) lanes contain purified sample eluted from a-M3DK magnetic beads. E) Left: survival probability curves of force ramp experiments of *K. marxianus* kinetochores (orange, median = 7.5 pN) and *S. cerevisiae* kinetochores (blue, median = 7.2 pN). Shaded regions represent the 95% confidence intervals. The survival curves differ significantly ($p = 0.04$ by log-rank test. Right: Scatter plots of individual rupture force values. Circles represent true ruptures and triangles represent escape events. Points are colored according to biological replicate.

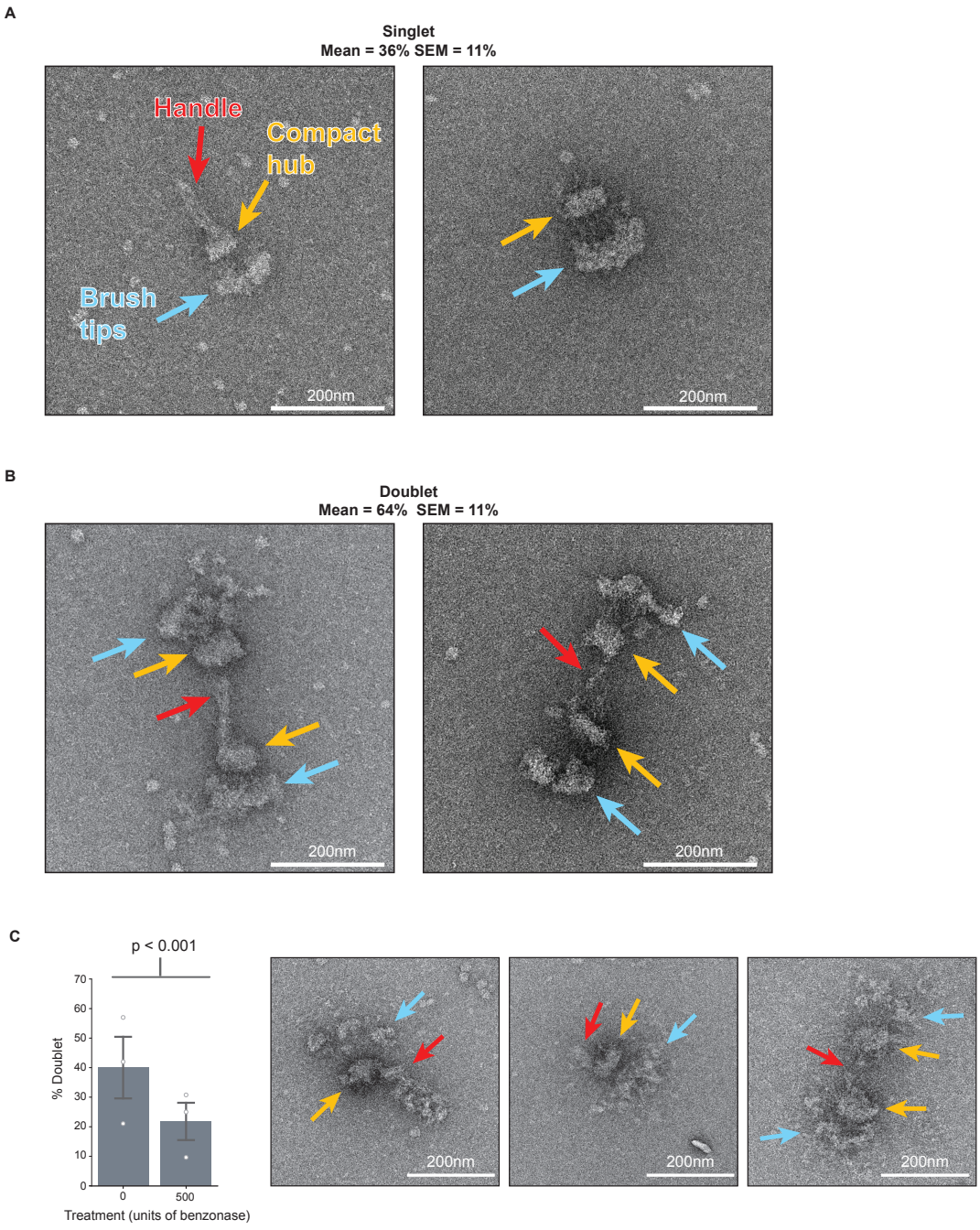

Figure 2. *K. marxianus* kinetochores have a paintbrush-like architecture and exist as singlets or doublets whose proportions can be changed by nuclease treatment. A) Two representative negative stain electron micrographs of singlet kinetochores exhibiting three major regions: the brush tips (blue arrows), the compact hub (yellow arrows), and the handle (red arrow). B) Two

representative negative stain electron micrographs of doublet kinetochores. Arrows indicate the same major regions as (A). Quantification of the proportion of doublet and singlet kinetochores was done for 50 kinetochores across 5 biological replicates. The mean percentages of doublets and singlets were 64% and 36%, respectively. C) Left - Graph represents the percent of doublet kinetochores visualized by negative stain EM when compared to the total amount for either a mock treated (0 units benzonase; n=181 kinetochores over 3 biological replicates; mean=40%; SEM=10%) or nuclease treated (500 units benzonase; n=223 kinetochores over 3 biological replicates; mean=22%; SEM=6.3%) samples. White dots represent biological replicates and gray bars represent standard errors of the means. P-value = 3.4×10^{-6} by chi-squared test. Right- representative images of kinetochores treated with 500 units of benzonase. Arrows indicate the same features as (A). Scale bars are 200 nm.

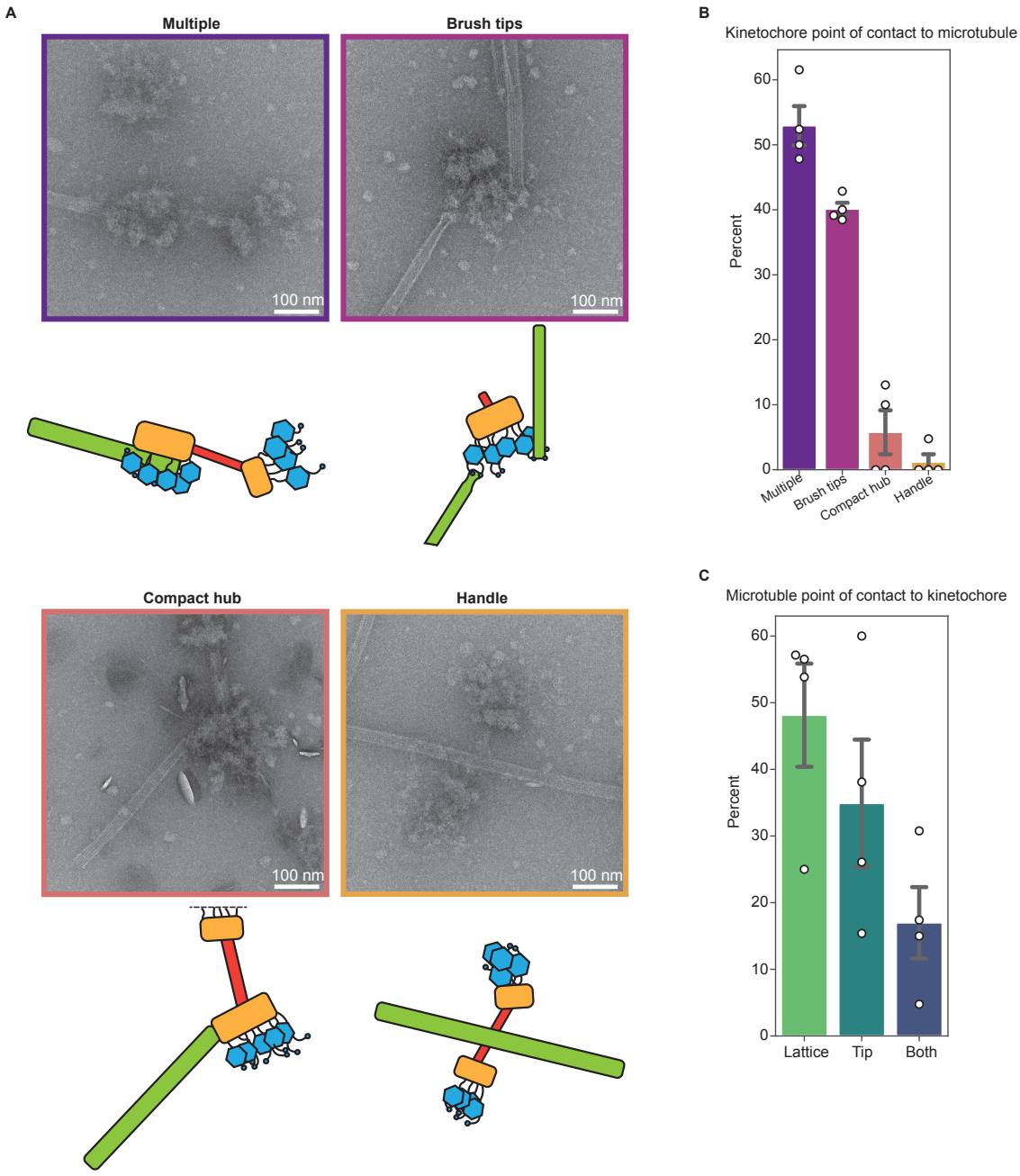

Figure 3. Kinetochores bind to the side and the ends of microtubules through the brush tips. A) Representative micrographs and corresponding cartoons showing multiple modes of interaction between kinetochores and taxol-stabilized microtubules. Images are representative of the categories in (B), and border colors correspond to the appropriate categories in (B). B)

Quantification of the percent of kinetochores seen interacting with the microtubule exclusively through the brush tips, handle, or compact hub. For (B) and (C) n=91 kinetochores across 4 biological replicates. The “multiple” category includes microtubule-bound kinetochores which appear to have multiple regions contacting the microtubule. White dots represent individual replicates. Gray bars represent the standard error of the mean. Mean percentages were as follows: multiple: 52.9%; brush tips: 40.1%; compact hub: 5.8%; handle: 1.2%. C) Left: Quantification of the percent of kinetochores interacting with the lattice, the tip, or both regions of microtubules. White dots represent individual replicates. Gray bars represent the standard error of the mean. Mean percentages were as follows: Lattice: 48.1%; tips: 34.9%; both: 17.0%. Scale bars represent 100 nm.

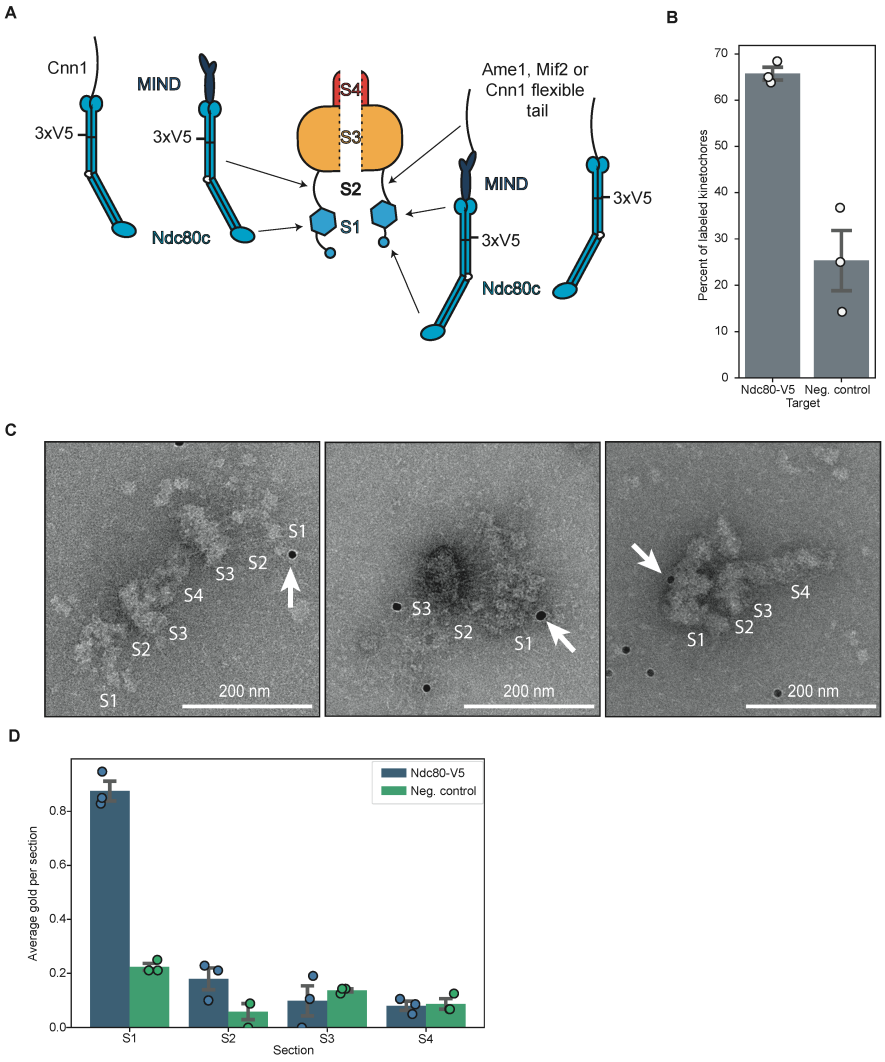

Figure 4. The major microtubule binding complex is in the distal brush tips. A) A cartoon schematic showing two possibilities for the location of Ndc80c. B) A graph showing the percent of kinetochores with at least one associated a-V5 gold particle relative to the total number of kinetochores. Kinetochores were purified from a strain with Ndc80-V5 epitope-tagged (Ndc80-V5, SBY21752; mean = 66%; st. dev = 3.3%) or not tagged (neg. control, SBY18150; mean=25%; st. dev=11%) and gold labeling was performed. Both groups contain 3 biological replicates. Error bars represent the standard error of the mean and white dots represent individual data points. C) Representative micrographs from gold labeling experiments targeting

Ndc80-V5 kinetochores. Kinetochores are broken into sections as in (A). White arrows indicate a gold label in contact with a kinetochore. Scale bars are 200 nm. D) Quantification of the average amount of gold labels found in each section of the kinetochore as illustrated in (A) across 3 biological replicates. Individual data points are represented by dots and error bars represent the standard error of the mean. Blue indicates the Ndc80-V5 sample while green indicates the negative control which contains no V5 tag.

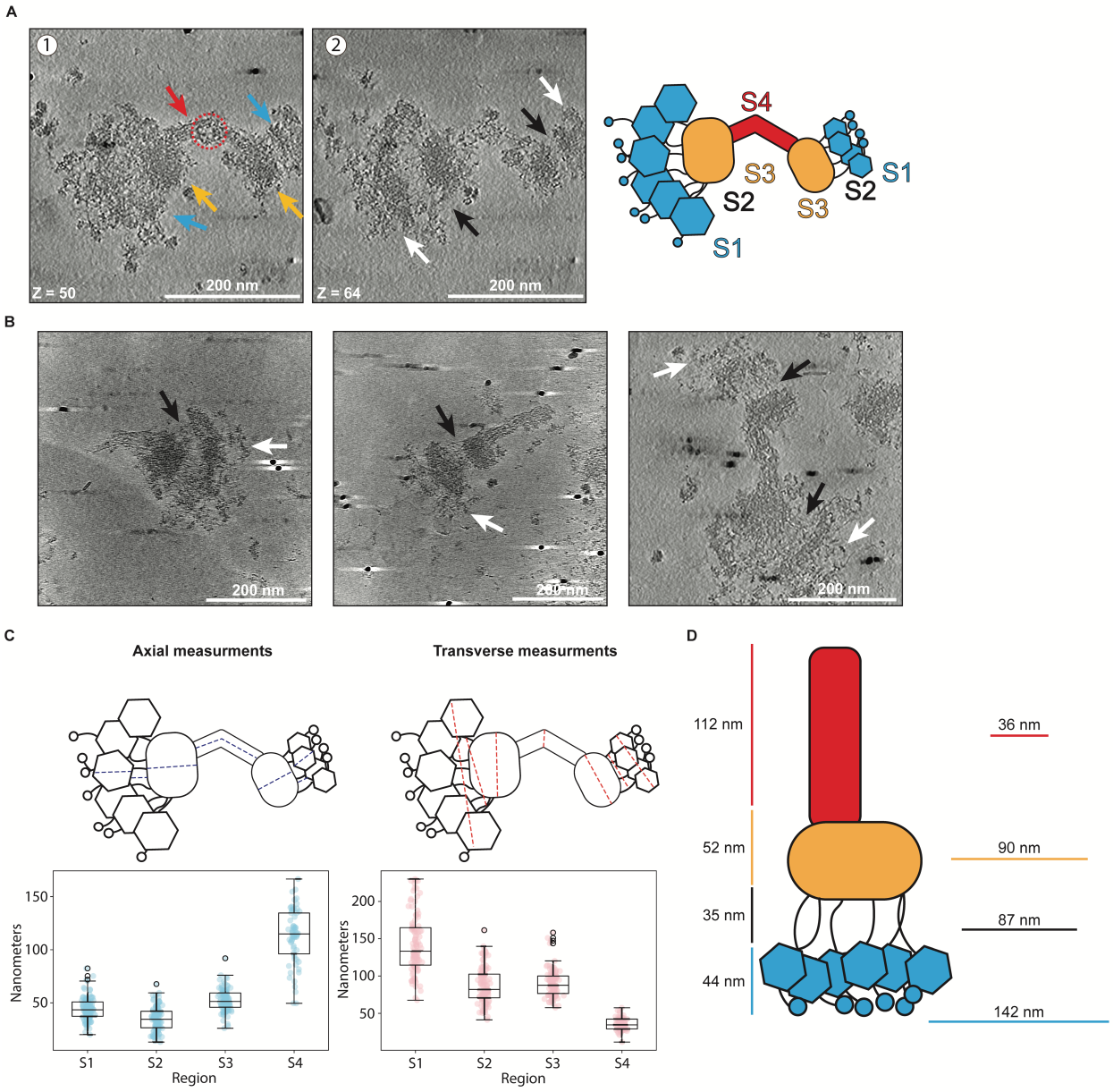

Figure 5. Cryo-electron tomography data reveals the major regions of kinetochore architecture. A) Two slices of a representative tomogram of a doublet kinetochore. 1: Arrows indicate the presence of the same major regions as seen by negative stain – the brush tips (blue), the compact hub (yellow) and the handle (red). The red dashed circle indicates the donut-like gap that could occasionally be seen in the handle. 2: Features which were not apparent in negative stain became more visible in ice. White arrows indicate brush tip extensions; black arrows

indicate flexible fibrils connecting the brush tips to the compact hub. Scale bars are 200 nm and Z slice numbers are indicated at the bottom left of each image. Each Z step is 1.056 nm. Far right: Schematic of kinetochore sections. B) Distance measurements of 101 kinetochores at the regions specified in the cartoon in (A) were taken axially (left) or transversely (right) and plotted as box plots. Colored dots indicate individual data points. Boxes indicate the interquartile range (25%-75%) with the median indicated by a black line inside the rectangle. Whiskers extend from the box to 1.5x the interquartile range, and outliers are indicated by white circles with black edges. C) Average kinetochore distance for each section. Axial measurements are to the left of the cartoon and transverse measurements are to the right. D) Example slices from tomograms of 3 different kinetochores. Black arrows indicate flexible fibrils and white arrows indicate brush tip extensions. Scale bars are 200 nm.

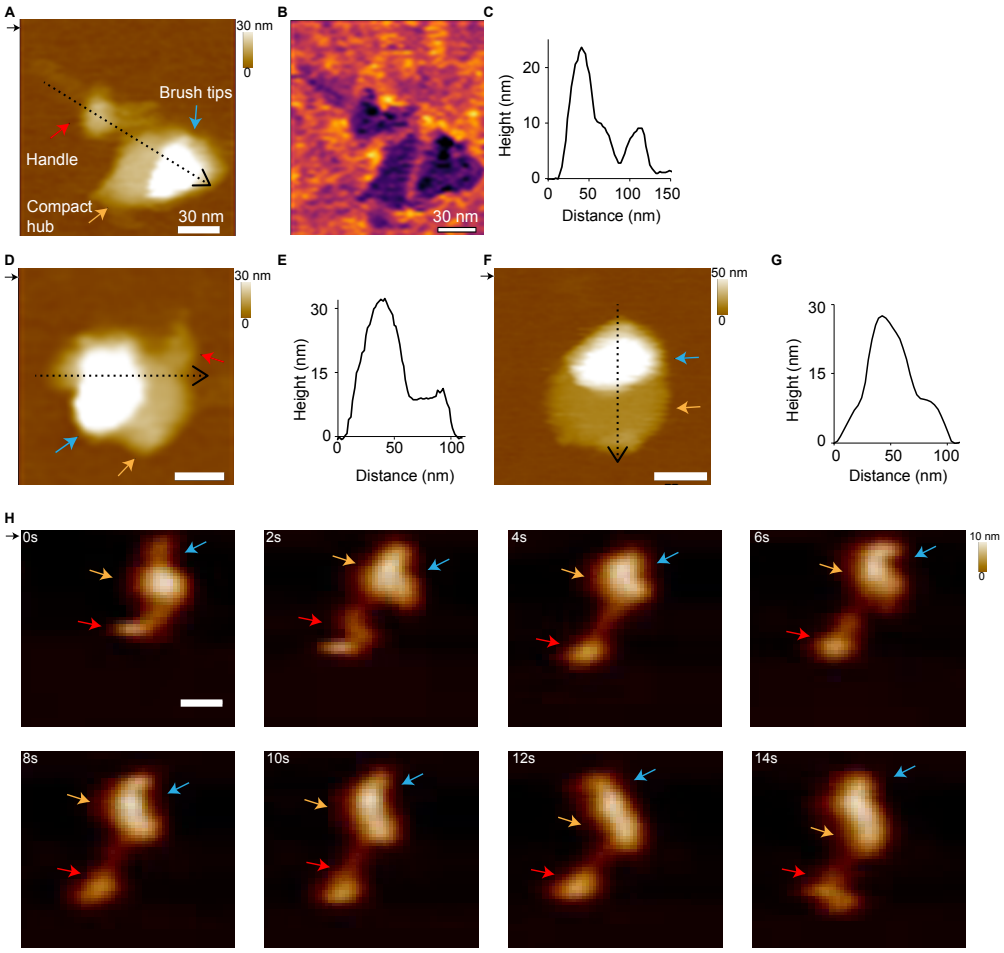

Figure 6. Atomic force microscopy confirms kinetochore shape and reveals dynamics. A) AFM height image of a kinetochore showing a paintbrush-like architecture with a long handle extending from a brush head. The red arrow indicates the brush handle, the orange arrow indicates the compact hub, and the blue arrow indicates the brush tips. B) The phase image from (A). C) The corresponding height profile taken along the dotted line in (A). D) AFM height image of a kinetochore showing the long brush handle close to the brush head. E) The corresponding height profile from the dotted line in (D). F) Height image of a kinetochore with just the brush head. G) The corresponding height profile from the dotted line in (F). H) Successive AFM height images showing the dynamics of individual kinetochores with significant

changes observed in the handle and the compact hub/brush tip regions over time (see Supplemental Movies 3 & 4). The direction of the scan is indicated by the small black arrow at the top left of the images. The scanning rate is 2 min/frame in (A, B, D, F) and ~1 s/frame in (H-I) with 256 x 256 pixels. The x-y scale bar is 30 nm. The z-scale is 0 to 30 nm (dark to light brown) in A and D, 0 to 50 nm in F, and 0 to 10 nm in H. The AFM image is colored according to height from the surface.

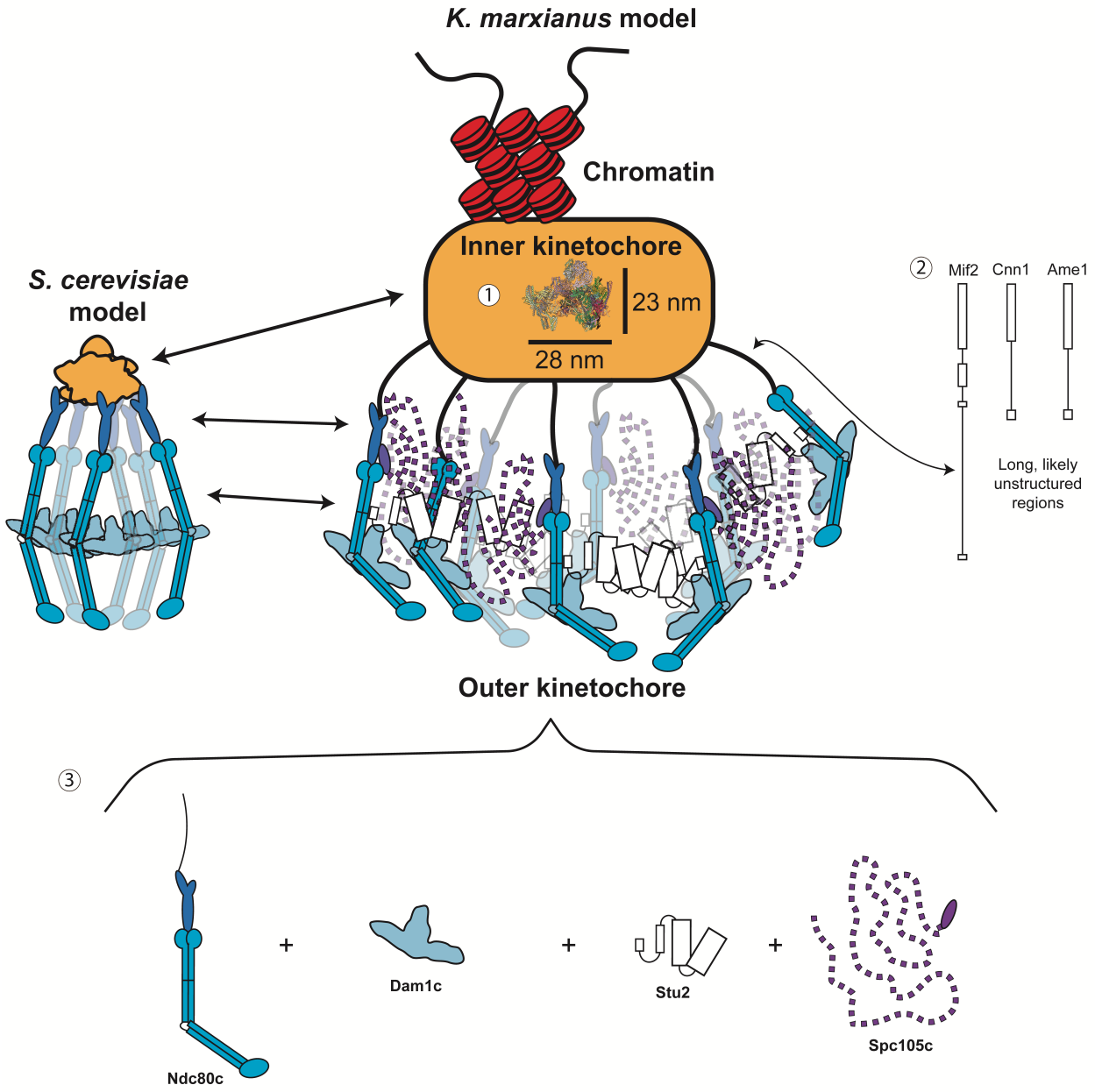

Figure 7. Key insights into global kinetochore architecture. A roughly to scale comparison of the size and overall architecture of the existing *S. cerevisiae* kinetochore model (left) compared to brush like particles of this work (right). Several features are highlighted by these kinetochores: 1- the inner kinetochore is buried within a dense mass large enough that published CCAN structures that include 2 CCANs and a nucleosome (PDB: 8OW1) can fit within its dimensions.

There is also an associated handle structure which contains exposed nucleic acid. 2- The connections between the inner and outer kinetochore are visible as long flexible fibrils which correspond to the long unstructured tails of the proteins responsible for making these connections (Mif2, Ame1, and Cnn1). 3- The major microtubule binder Ndc80c is located in the brush tips. Its interaction with various large and often flexible binding partners creates large clouds of proteins capable of binding microtubules and regulating those interactions.

2.7 Supplemental figures & legends

Complex	Protein	*S. cerevisiae* molecular weight (kDa)	Expected molecular weight of *K. marxianus* homolog (kDa)	*K. marxianus* protein sequence ID	Alignment score to *S. cerevisiae*	E. value
Ndc80c	Ndc80	80.5	78.4	XP_022677987.1	551	0.0E+00
	Nuf2	52.9	52.9	XP_022676124.1	393	2.0E-138
	Spc24	24.6	20.9	XP_022675266.1	47	2.0E-11
	Spc25	25.2	25.2	XP_022673631.1	89.4	1.0E-26
Spc105	Kre28	44.7	41.1	XP_022673577.1	60.5	1.0E-14
	Spc105	105	97	XP_022677423.1	184	3.0E-52
Dam1c	Hsk3	8.09	7.3	XP_022675267.1	44.3	4.0E-13
	Dam1	38.4	38.9	XP_022677914.1	158	3.0E-50
	Duo1	27.5	22.9	XP_022673782.1	94.4	2.0E-28
	Spc19	18.9	17.7	XP_022678124.1	80.1	2.0E-26
	Spc34	34.1	32.3	XP_022676083.1	177	5.0E-59
	Dad2	15.1	13.7	XP_022673936.1	97.1	6.0E-32
	Dad4	8.16	8.5	XP_022677868.1	102	3.0E-36
	Ask1	32	26.7	XP_022678310.1	113	1.0E-34
	Dad1	10.5	11.9	XP_022676704.1	99.8	6.0E-34
	Dad3	10.8	9.5	XP_022674564.1	79	4.0E-26
MIND	Nnf1	23.6	23.6	XP_022677716.1	140	7.0E-47
	Dsn1	65.7	63.2	XP_022676920.1	43.5	1.0E-08
	Nsl1	25.4	25.7	XP_022677830.1	144	6.0E-48
	Mtw1	33.2	33.4	XP_022676573.1	228	2.0E-78
Stu2	Stu2	101	97.9	XP_022677161.1	420	3.0E-137
Ctf19c	Iml3	28.1	-	-	-	-
	Chl4	52.7	45.3	KAG0682270.1	116	6.0E-34
	Nkp1	27	24.3	XP_022674906.1	36.2	2.0E-07
	Nkp2	17.9	17.6	BAP71547.1	19.6	1.4E-02
	Ame1	37.4	33	XP_022673771.1	64.3	3.0E-16
	Okp1	47.3	51.2	XP_022675341.1	118	7.0E-34
	Ctf3	84.3	71.9	XP_022677695.1	160	8.0E-31
	Mcm16	21.1	18.8	XP_022677702.1	42.7	3.0E-10
	Mcm21	43	34.8	XP_022675474.1	70.9	3.0E-18
	Mcm22	27.6	26.1	XP_022676344.1	69.7	4.0E-19
	Cnn1	41.3	30.2	QGN15715.1	-	-
	Wip1	10.2	10.2	XP_022674922.1	24.6	5.0E-05
	Mif2	62.4	60.9	XP_022675205.1	333	4.0E-112
Cbf3	Ndc10	112	88	XP_022674868.1	239	4.0E-71
	Cep3	71.4	72.2	XP_022674990.1	273	1.0E-87
	Ctf13	56.3	46	XP_022674481.1	129	1.0E-37
	Skp1	22.3	20.9	XP_022677187.1	282	4.0E-103
Cbf1	Cbf1	39.4	40.6	QGN15070.1	166	1.0E-52
Cse4	Cse4	26.8	22.4	XP_022678314.1	192	3.0E-67

Supplementary Table 1. A table of *S. cerevisiae* kinetochore proteins and their homologs in *K. marxianus* identified by mass spectrometry. Proteins which were identified in the mass spectrometry data are in white rows. Proteins which were not identified in our mass

spectrometry but were found by BLAST search of NCBI taxID:4911 using the *S. cerevisiae* protein as a reference are colored green. Proteins which were found by BLAST search of NCBI taxID: 4911using a *Kluyveromyces lactis* protein as reference are colored blue. Proteins for which no homolog was found are colored red. Alignment scores and Expected values are listed, where higher alignment scores and lower E. values indicate better matches.

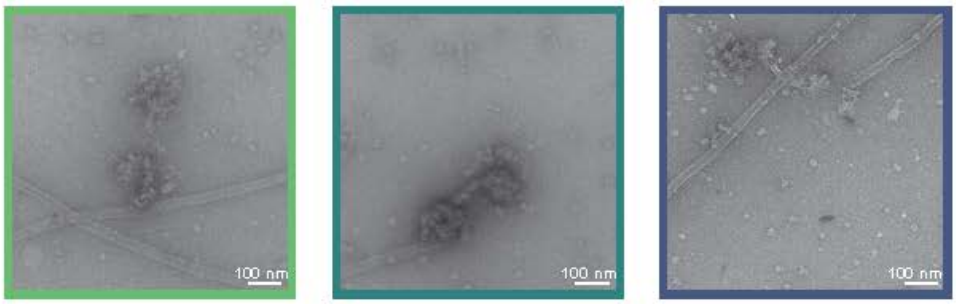

Supplemental Figure 1. Representative images of kinetochores interacting with microtubules on either the lattice (left), tip (center), or both (right). Scale bars are 100 nm.

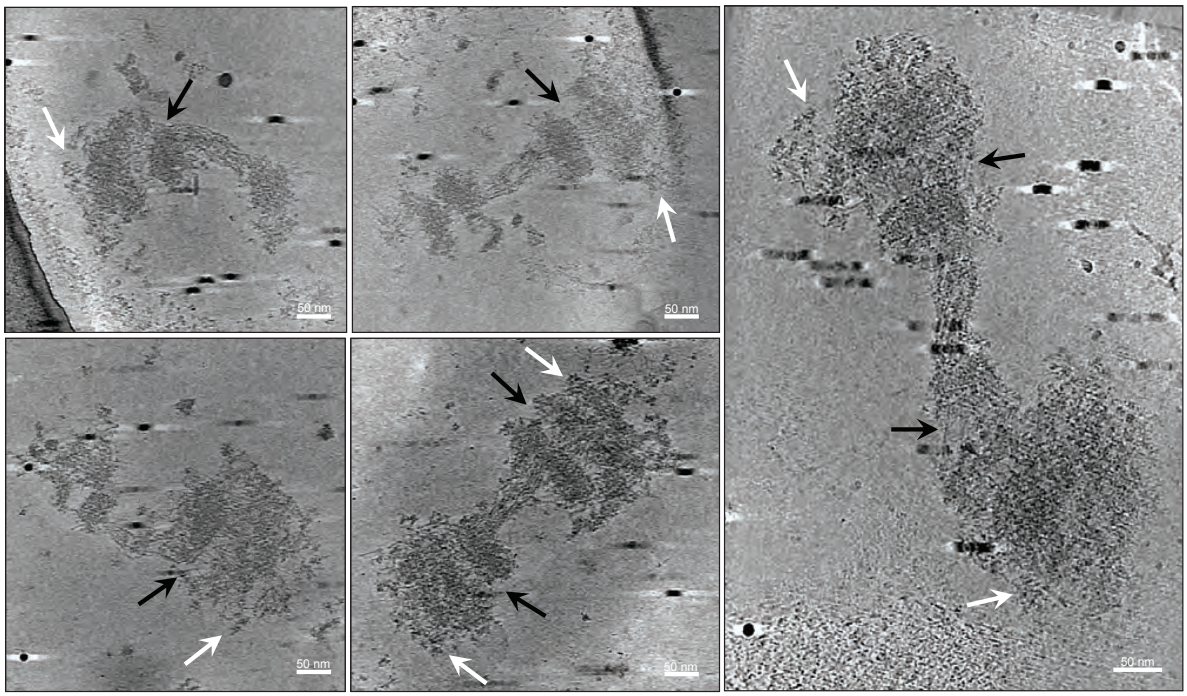

Supplemental Figure 2. Gallery of kinetochores revealed by cryo-electron tomography. Black arrows: flexible fibrils connecting the brush tips to the compact hub. White arrows: brush tip extensions. Scale bars are 50 nm in each panel.

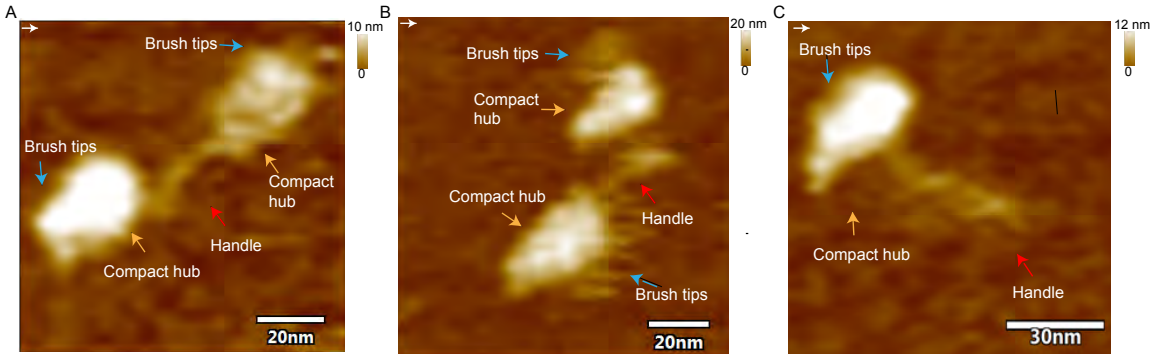

Supplemental Figure 3. Three examples of AFM height images of double kinetochores. The blue arrows indicates the brush tips, the orange arrows indicates the compact hub, and the red arrow indicates the brush handle. The x-y scale bar is 20 nm. The scanning rate is 1 s/frame with 256 x 256 pixels. White arrows at the top left of the images indicate the scanning direction. The z-scale is 0 to 20 nm (dark to light brown).

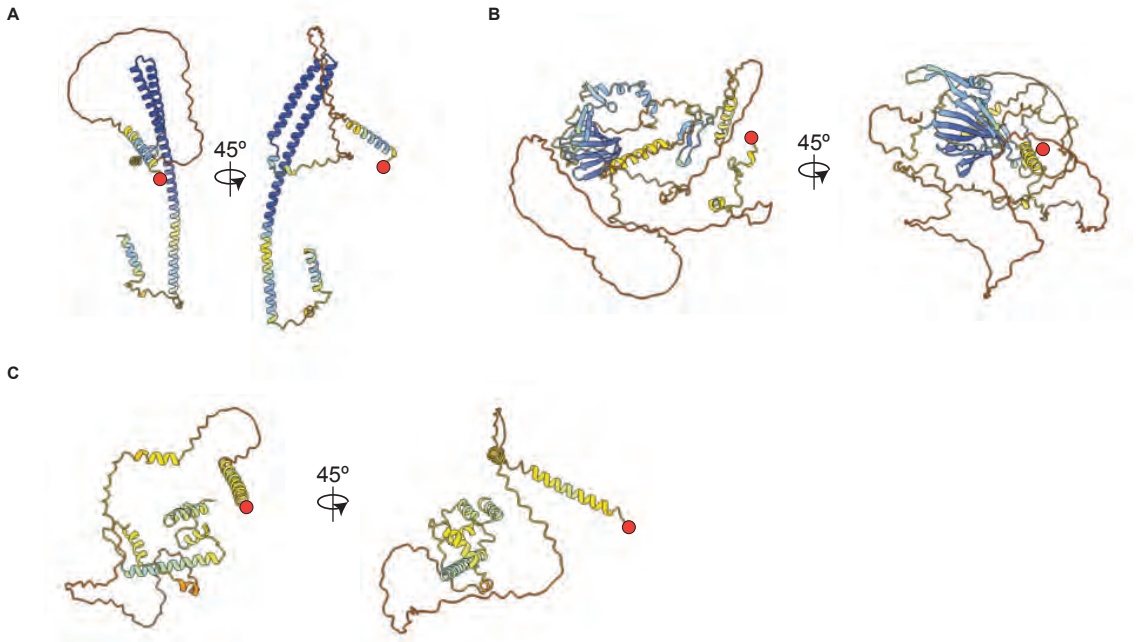

Supplemental Figure 4. Alphafold ColabFold predictions of Ame1, Mif2, and Cnn1 show long disordered tails. A) A structural prediction for K. marxianus Ame1 with its N-terminus marked with a red circle. B) A structural prediction for K. marxianus Mif2 with its N-terminus marked with a red circle. C) A structural prediction for the potential K. marxianus Cnn1 homolog with its N-terminus marked with a red circle. All models are colored by per-residue confidence score (pLDDT) where blue indicates high confidence and red indicates low confidence.

Chapter 3: *K. marxianus* utilizes a point centromere despite doublet kinetochores

At time of writing, the contents of this chapter are under review for publication with the following authors and corresponding contributions:

Authors: Daniel J. Barrero, Sabrine Hedoin, Charles L. Asbury, Andrew Stergachis, Eileen O'Toole, Sue Biggins.

3.1 Summary

Cells must duplicate and segregate their genetic information in order survive. In eukaryotes the segregation of chromosomes occurs through the interaction of two dynamic structures within the cell. The first is the mitotic spindle, a cytoskeletal system that uses microtubules to contact and position the chromosomes, and the second is the kinetochore, a large protein machine that assembles directly on the centromere of chromosomes and binds dynamic microtubule tips[7,79]. Together these allow chromosomes to be moved to the correct end of the cell during mitosis. We previously established a purification of native kinetochores from the yeast *Kluyveromyces marxianus* in order to study kinetochore architecture[140]. Surprisingly, a portion of those purified kinetochores appeared linked into a doublet, leading us to question if it shared the same point centromere construction as the related model organism *Saccharomyces cerevisiae*[15]. In the following work we demonstrate that though the doublet kinetochores have a functional impact on kinetochore strength, kinetochore localization throughout the cell cycle appears conserved between these two yeasts and whole spindle reconstructions indicate the presence of a point centromere.

3.2 Introduction

Accurate replication and partitioning of genetic material during cell division is essential to life. Eukaryotes achieve this through a massive protein machine called the kinetochore, which assembles directly on chromosomes and attaches to microtubules to segregate chromosomes during mitosis[37,79]. Errors in chromosome segregation are a hallmark of cancers and many developmental diseases[141-143]. The region of DNA onto which the kinetochore assembles is called the centromere, which in *Saccharomyces cerevisiae* is defined by a roughly 125-bp DNA sequence that forms a centromeric nucleosome with a histone variant called Cse4 (Cenp-A in humans)[41,42,144] . In *S. cerevisiae*, the centromere assembles a single kinetochore unit, which in turn binds a single microtubule emanating from the spindle pole body (SPB)[15]. This simple system is referred to as a point centromere. In contrast, human centromeres are regional and are composed of many copies of repetitive α-satellite DNA which can assemble many kinetochore units, which then in turn bind between 10-15 microtubules[95,145]. This system is referred to as a regional centromere. Because of their relative simplicity, budding yeast are a powerful model system for kinetochore biology. Despite these differences, the kinetochore components themselves are structurally well conserved between yeast and humans, and the kinetochore units in regional centromeres are thought to closely resemble the kinetochores of point centromeres[49,104,105,146].

The yeast kinetochore itself can be divided into two sections, inner and outer. Two copies of the inner kinetochore CCAN complex assemble directly onto the centromere and make contact with both Cse4 and the centromeric DNA[49,50,105,147] . Several members of the CCAN complex then bind the outer kinetochore through long, unstructured tails[59,60,148]. The principal function of the outer kinetochore is to bind dynamic microtubules from the mitotic spindle, harnessing the movement generated by their assembly and disassembly to carry the chromosome to the correct end of the cell[72,109,110]. The exact copy number of outer kinetochore

complexes is an ongoing area of study, but estimates range between 4 and 12, and that number fluctuates with the stages of mitosis[113-116,149]. In *S. cerevisiae*, kinetochores remain assembled and bound to microtubules except for a small window during S phase[150].

The microtubules to which yeast kinetochores bind emanate from one of two spindle pole bodies (SPB), functionally equivalent to centrosomes in animals[151]. The *S. cerevisiae* SPB appears as a trilaminar disk embedded within the nuclear membrane, which does not break down during mitosis[9,152]. The hallmark layers of the SPB consist of an outer plaque that faces the cytoplasm and nucleates cytoplasmic microtubules, a central plaque that spans the nuclear membrane, and an inner plaque that faces the nucleoplasm and nucleates kinetochore microtubules as well as inter-polar microtubules that are important for SPB positioning[9,152].

To understand how kinetochores achieve their unique functions it is critical to understand their architecture. Native kinetochore particles can be readily purified from *S. cerevisiae* and have proven invaluable for biophysical and biochemical analysis[86,87,91]. However, it has been difficult to examine the architecture of these particles with structural methods due to their strong tendency to fall apart on electron microscopy grids[92]. To surpass this, our group purified native kinetochore particles from the thermotolerant budding yeast *Kluyveromyces marxianus* as the adaptations evolved to live at high temperature tend to create more stable proteins that can be used for structural methods[120-122]. We were able to purify and visualize kinetochores from this organism through negative stain electron microscopy, cryo-electron tomography, and atomic force microscopy. We further showed that these kinetochores bind microtubules, and localized both the major microtubule binder Ndc80c and the inner kinetochore within these particles[140].

Surprisingly, kinetochores purified from *K. marxianus* appear as a mixture of singlets and doublets and nuclease (benzonase) treatment reduces the doublet population, suggesting they are tethered by DNA[140]. This suggested that in contrast to the well established point centromere of *S. cerevisiae*, *K. marxianus* may utilize a small regional centromere capable of assembling two kinetochore units. We demonstrate that the doublet kinetochores have a significant impact

on kinetochore strength, consistent with the possibility of regional centromeres. We also show using fixed cell fluorescence microscopy that doublet and singlet kinetochores can fit within pre-anaphase mitotic spindles in this organism. To directly determine the amount of microtubule per centromere, and thus determine a point versus regional centromere, we tomographically reconstructed whole mitotic spindles from logarithmically growing cells. and rule out the possibility that they represent a small regional kinetochore by reconstructing *K. marxianus* spindles in vivo. These reconstructions reveal too few microtubules per spindle pole to account for regional centromeres.

3.3 Results

3.3.1 Kinetochore doublets impact microtubule attachment strength

If both units of a doublet kinetochore can fold together to interact with a single microtubule, this might correspond to a higher strength interaction between the kinetochore and the microtubule. We therefore asked if benzonase-treated kinetochores behave differently from untreated controls in our previously established optical trapping assay that assesses the functional strength of kinetochores[86,140].

To purify kinetochores from K. marxianus we employed a previously described strain in which the *DSN1* gene had been endogenously tagged with 6xHis and 3xM3DK (Dsn1-His-M3DK)[140]. Logarithmically growing cells were treated with benomyl to suppress microtubule dynamics and enrich for mitotic cells, reducing cell cycle stage variability. Benzonase and α-M3DK beads were added to cell lysate for 3 hours, after which the beads were removed and thoroughly washed, and kinetochores were eluted with M3DK peptide. Benzonase treatment did not dramatically alter kinetochore composition as assayed by SDS-PAGE, which demonstrated the retention of almost all protein bands in the benzonase treated sample except bands above 150 kD (Fig. 1A). Kinetochore components are not predicted to be greater than 150 kD, but we

further analyzed the kinetochore composition after benzonase treatment. First, we confirmed the presence of the outer microtubule binding complexes Ndc80c and Dam1c members mass spectrometry (Fig. 1B). Thus, though the proportion of doublets is reduced with benzonase treatment, the overall protein composition of the kinetochores remains consistent.

We performed optical trapping on the kinetochores treated with and without benzonase. Despite their similar composition, benzonase-treated kinetochores were significantly weaker than untreated controls (Fig 1C, D; $p < 0.005$ by log-rank test). The benzonase treated kinetochores also lost the bimodal distribution present in untreated controls, and became functionally indistinguishable from *S. cerevisiae* kinetochores (Fig 1D, $p = 0.77$ by log-rank test). These results suggest the loss of doublets has a functional impact on kinetochore strength, and is consistent with a potential regional centromere.

3.3.2 Kinetochore positioning throughout mitosis is consistent between *K. marxianus* and *S. cerevisiae*

Given the potential of a significantly different centromere construction compared to *S. cerevisiae,* we sought to determine if well established morphological features of the cell cycle were conserved in *K. marxianus*. Work in *S. cerevisiae* has found that kinetochores remain attached to microtubules throughout the cell cycle, clustering into a focus which then separates into two foci during cell division. Because *K. marxianus* has yet to be characterized in this manner we first wanted to check if this clustering was indeed present. We therefore epitope tagged the outer kinetochore gene *DAD1* at the endogenous locus with the fluorophore mKate2 (Dad1-mKate2). Logarithmically growing Dad1-mKate2 cells were fixed with formaldehyde, DAPI stained, and examined by microscopy. Cells were visible in all stages of budding, indicating active progression through the cell cycle (Fig 2A). As in *S. cerevisiae*, unbudded cells showed a single focus of Dad1 fluorescence that was localized to a single mass of DNA (Fig. 2A, unbudded). Small-budded cells maintained a single kinetochore focus and amorphous

nuclear DNA signal (Fig. 2A, small-budded). Occasionally, small-budded cells could be seen with two kinetochore foci, indicating spindle formation and entry into mitosis. In large-budded cells, two kinetochore puncta were clearly visible. Large-budded cells were categorized as pre-anaphase if their DNA was rounded, and anaphase if it was elongated (Fig 2A, large-budded/pre-anaphase, large-budded/anaphase). Pre-anaphase inter-kinetochore distance measurements had a median distance of 0.420 μm (Fig 2B).

Sister kinetochores must be able to fit within the inter-kinetochore distances measured above. We therefore compared the distribution of end-to-end length measurements from previously published cryo-electron tomographic (cryo-ET) data and compared it to the distribution of inter-kinetochore distances (Fig. 2C). The cryo-ET doublet kinetochore lengths (375 nm, n=31 doublet kinetochores) easily fit within the spread of inter-kinetochore distances, and cluster within 100 nm of the median inter-kinetochore distance (Fig. 2B, 420 nm, n=274 measurements). Thus, kinetochore positioning through mitosis is consistent between *S. cerevisiae* and *K. marxianus.*, and kinetochores can fit between the measured inter-kinetochore distances.

3.3.5 Spindle reconstructions indicate a point centromere

If *K. marxianus* employs a regional centromere, there would be two microtubule binding sites for each centromere. To test this, we reconstructed whole mitotic spindles from logarithmically growing *K. marxianus* cells. As shown previously, electron tomography provides a detailed view of spindle morphology in yeast cells because it allows for the clear resolution of individual microtubules and spindle poles[9,153]. We therefore prepared cells by High Pressure Freezing and Freeze Substitution (HPF/FS) and collected electron tomograms to reconstruct their spindles. We expected the spindle pole body (SPB) to appear similarly to that of *S. cerevisiae*, as a tri-laminar disk with a heavy staining central plaque embedded within the nuclear membrane and an inner and outer plaque from which nuclear and cytoplasmic

microtubules emanate. Indeed, structures resembling the *S. cerevisiae* SPB were readily identifiable in the nuclear membrane of dividing cells (Fig. 3A). The central layer, commonly referred to as the central plaque, is embedded in the nuclear envelope and has a layered structure similar to *S. cerevisiae* (Fig. 3A, yellow arrows). However, the SPB is consistently smaller in size with an average diameter of 66 nm compared to roughly 100 nm in *S. cerevisiae*. Mother SPBs in *K. marxianus* also seemed to assemble a tilted outer plaque on the cytoplasmic face (Fig. 3A, blue arrows) and half bridges were visible (Fig. 3A; green arrows). To reconstruct the spindle, we focused on microtubules originating in the SPB and extending into the nucleus. For microtubules with discernable plus ends, we were able to make out limited tip morphology, including some examples of protofilament flares (Fig. 3B).

Nine mitotic spindles were reconstructed, measuring from 0.6 μm to 3.38 μm in length, defined as the SPB to SPB distance (Fig. 3C). The four short spindles (defined as less than 1 μm long) and one medial (~1 μm) spindle averaged 27 microtubules total, with individual SPBs containing between 10 and 15 microtubules (Fig 3D). Published data from *S. cerevisiae* shows that short and medial spindles can contain 38-43 spindle mts[15]. Four of the spindles were in late anaphase, and for three of those we reconstructed only a half spindle. The complete late anaphase spindle contained 15 microtubules total, 8 from one spindle pole and 7 from the other (Fig. 3D). This is in stark contrast to published data from *S. cerevisiae* where the anaphase B spindle contains ~39 mts[15]. The reduced number of microtubules compared to *S. cerevisiae* is consistent with the smaller SPBs, as SPB surface area tends to scale with number of microtubules[154].

The *K. marxianus* spindles were consistently shorter than *S. cerevisiae* spindles of similar stage. The majority of microtubules were short and near the spindle pole, with a few extending across the spindle, possibly as interpolar microtubules important for creating and maintaining the separation between spindle poles rather than kinetochore binding. By the time the spindles reached late anaphase, indicated by the nucleus spanning the mother and

daughter cell, the number of microtubules visible per spindle decreased to between 6 and 8 per pole (Fig 3D, late anaphase spindles). Of these, 1 to 2 microtubules tend to be very long interpolar microtubules, with the rest remaining short and near their respective pole. Considering *K. marxianus* has 8 chromosomes, these spindle reconstructions are most consistent with roughly one microtubule per kinetochore and a few additional microtubules to serve as interpolar microtubules.

3.4 Discussion

Here we report the centromeric and spindle organization of *K. marxianus*. Initial observations suggested a regional centromere by the existence of doublet kinetochores. These doublets impacted the strength of the kinetochores, consistent with both kinetochore units being able to interact with microtubules as in a regional centromere. This suspected difference from *S. cerevisae* prompted us to examine kinetochore localization and cell morphology throughout the cell cycle in order identify other potential differences. Instead, kinetochore localization and the budding process were similar to *S. cerevisae*. To more definitively settle the question of a point versus regional centromere we reconstructed whole mitotic spindles from electron tomograms. These reconstructions revealed an insufficient number of microtubules per chromosome to result in regional centromeres. Thus, despite the appearance of double kinetochores *K. marxianus* utilizes a point centromere.

The evidence of a point centromere is nicely consistent with findings in *S. cerevisiae*, however the question as to the role and origin of the doublet kinetochores previously reported remains. An intriguing possibility is that a small regional centromere does in fact exist and assembles two kinetochore units, however both of these units are capable of interacting with a single microtubule. In this sense, the tomographic reconstructions cannot rule out a centromere that contains multiple kinetochore units but interacts only with a single microtubule. However,

preliminary data in our lab suggests this is not the case. Fiber-seq analysis measuring the accessibility of DNA, which can be interpreted as read out for nucleosome positioning, shows an inaccessible stretch of DNA at the *K. marxianus* centromere that is only slightly longer than the protected centromeric DNA in *S. cerevisiae.* This suggests that there is in fact only a single Cse4 nucleosome at the *K. marxianus* centromere, and thus we expect only a single kinetochore unit assembles as in *S. cerevisiae*.

Another possibility is that a subset of sister kinetochores remained linked throughout our kinetochore purification process, and these are the doublets. This seems an unlikely possibility as cohesin, the complex responsible for linking sister chromatids during mitosis, is not present in the previously reported mass spectrometry analysis of these kinetochore purifications[140].

It is also possible that the doublets are an artifact of the purification protocol. These kinetochore purifications require long incubations of beads in lysate, during which time free floating kinetochores may be subject to DNA ligase activity. Previous work has established that *K. marxianus* has very efficient non-homologous end-joining machinery, and other groups have had to disrupt this machinery in order to create genetically tractable strains[155]. This machinery may ligate exposed DNA ends present near the inner kinetochore, resulting in the doublets. In the future inhibiting DNA ligase activity in lysates, either by chemical inhibitors or other methods, will be an important step in elucidating the origin of the doublets.

3.5 Materials and methods

Strain construction

The *Saccharomyces cerevisiae* strain used in this study is SBY8253 (*DSN1-6xHis-3xM3DK:URA3*) and was derived from the W303 background and was previously described[16]. The *Kluyveromyces marxianus* strains used in this study are SBY18150 (*DSN1-6xHis-3xM3DK:KanMX*) and SBY22682 (DAD1-mKATE2:KanMX), and were derived from SBY17411 (NRRL Y-8281, USDA ARS culture collection). All strains were tagged at the endogenous locus.

Briefly, DNA fragments of either 500 or 1000 bases immediately upstream and downstream of the desired integration site were generated from genomic DNA. A backbone plasmid was selected based on the desired tags, and the fragments amplified from genomic DNA were inserted into the backbone plasmid via Gibson assembly such that each plasmid contained a restriction site, followed by 500 to 1000 base pairs of upstream homology, followed by the desired tags and markers, followed by 500 to 1000 base pairs of downstream homology, followed by another restriction site. Plasmids were then digested and transformed into the desired strain for integration by homologous recombination. Successful integration was confirmed by PCR and immunoblotting. The plasmids (pSB prefix) and yeast strains (SBY prefix) used are as follows: SBY18150 contains plasmid pSB2951 generated with primers SB5736, SB5737, SB5738, SB5739, transformed into SBY17411. SBY22682 contains plasmid pSB3501 generated with primers SB8274, SB8275, SB8276, SB8277, SB8278, SB8279, transformed into SBY17411. All tagged strains grow similarly to the parent strain.

Yeast growth and kinetochore purification for optical trapping

All yeast growth was performed as described previously[16]. Briefly, yeast were grown in YPD (1% yeast extract, 2% peptone, 2% D-glucose). SBY18150 cultures were grown in the presence of 200 µg/ml G418. Large cultures were grown on shakers (220 rpm) at 22 °C or 30 °C for *S. cerevisiae* and *K. marxianus,* respectively. Cultures were treated with benomyl at a final concentration of 30 µg/ml (1:1 addition of 60 µg/ml benomyl YEP media) for 2 hours at 23 ˚C and then harvested by centrifugation for 10 minutes at 5000xg at 4 ˚C. Kinetochores were purified as previously described[16]. Briefly, the endogenous *DSN1* kinetochore gene was C-terminally tagged with 6xHis and 3xM3DK. Harvested yeast were resuspended in Buffer H (25 mM HEPES pH 8.0, 150 mM KCl, 2 mM MgCl2, 0.1 mM EDTA pH 8.0, 0.1% NP-40, 15% glycerol) supplemented with protease inhibitors, phosphatase inhibitors, and 2 mM DTT. After resuspension and re-spinning, yeast pellets were frozen in liquid nitrogen and lysed using a Freezer Mill (SPEX, Metuchen NJ). Lysate was clarified via ultracentrifugation at 24,000 RPM

(98,000 x g) for 90 minutes and the protein layer was extracted with a syringe. This extract was incubated with magnetic a-M3DK antibody conjugated Dynabeads (Invirtrogen, Waltham MA) for 3 hours at 4 °C with rotation. For benzonase treated samples 300 units of benzonase per milliliter of lysate were added during this incubation step. Dynabeads were washed with 10x bead volume of Buffer H 5 times (the last 3 washes omitting DTT and phosphatase inhibitors). Kinetochores were eluted with 0.5 mg/ml 3xM3DK peptide in Buffer H lacking DTT and phosphatase inhibitors. For mass spectrometry, kinetochores were eluted from Dynabeads with 0.2% RapiGest (Waters Corporation, Milford MA) in 50 mM HEPES pH 8.0. For all experiments, the total protein concentration was determined by NanoDrop measurement and purity by silver stain gel analysis.

Optical trapping

Optical trapping rupture force assays were performed as previously described[16]. Streptavidin coated 440 nm polystyrene beads (Spherotech, Lake Forest IL) were functionalized with biotinylated anti-penta-His antibody (Qiagen, Hilden Germany or R&D Systems, Minneapolis MN) and stored in BRB80 containing 8 mg/ml BSA and 1 mM DTT at 4 °C with continuous rotation. Beads were decorated with purified kinetochores (via Dsn1-6His-3M3DK) in a total volume of 20 µl incubation buffer (BRB80 containing 1.5 mg/mL κ-casein). To ensure sparse decoration of the beads and reduce the likelihood of multiple kinetochore-microtubule interactions being measured simultaneously, we empirically determined kinetochore concentrations such that roughly 1 in 10 beads exhibited microtubule binding activity during the assay. Dynamic microtubule extensions were grown from coverslip-anchored GMPCPP-stabilized microtubule seeds in a microtubule growth buffer consisting of BRB80, 1 mM GTP, 250 µg/ml glucose oxidase, 25 mM glucose, 30 µg/mL catalase, 1 mM DTT, 1.4-1.5 mg/mL purified bovine brain tubulin and 1 mg/mL κ-casein. Assays were performed at 23 °C. Rupture force experiments were performed as in[16]. Briefly, an optical trap was used to apply a force of ~1-2 pN in the direction of microtubule assembly. Once beads were observed to track with

microtubule growth for roughly 30 seconds (to ensure end-on attachment), the applied force was increased at a constant rate of 0.25 pN/s until bead detachment. Records of bead position over time were generated and analyzed using custom software (LabVIEW and Igor Pro, respectively) and used to determine the rupture force, which was marked as the maximum force sustained by the attachment during each event.

Cell fixation and Microscopy

Briefly, SBY22682 cultures were grown in YPD (1% yeast extract, 2% peptone, 2% D-glucose) at 22°C. 1ml was removed during mid-log phase growth (~OD 0.6) and yeast were pelleted by centrifugation at 21,000xg for 1 minute. Supernatant was removed and the yeast pellet was resuspended in 1ml 0.1M potassium phosphate pH 6.4 with 3.7% formaldehyde for fixation. This mixture was incubated at room temperature for 10 min before centrifugation at 21,000xg for 1 minute. Supernatant was removed and fixed cells were resuspended in 1ml 0.1M potassium phosphate pH 6.4 and stored at 4°C for up to two weeks. Immediately prior to imaging cells were pelleted with the same spin parameters and resuspended in 100µl DAPI staining buffer (1.2M sorbitol, 1% Triton-X100, 0.1M potassium phosphate pH 7.5, 2µg/ml DAPI) for 10 minutes. Cells were then pelleted again and resuspended in 100µl imaging buffer (1.2M sorbitol, 1% Triton-X100, 0.1M potassium phosphate pH 7.5). Cells were applied to microscope slides with thin agarose pads[156].

Fixed cells were imaged using a Deltavision Ultra deconvolution high resolution microscope with a 100x/1.42 PlanSApo oil immersion objective (Olympus Life Science, Waltham, MA). Images were collected with a 16-bit sCMOS detector. Cells were imaged using Z-stacks with 0.2µm steps through the entire cell. Deconvolution was done using standard settings through SoftwoRX software. All quantification was done using ImageJ (National Institutes of Health).

Tomography

Cells were prepared for electron tomography using high pressure freezing followed by freeze substitution as previously described[9,157,158]. Briefly, logarithmically growing *K. marxianus* cells were collected by vacuum filtration and frozen using a Leica EMPact2 high pressure freezer (Leica Biosystems, Deer Park IL). The frozen cells were then freeze substituted in 1% OsO_4 and 0.1% uranyl acetate in acetone and embedded in epon. Thick (250 nm) sections were collected onto formvar-coated slot grids. The grids were then stained post-stained with 2% uranyl acetate followed by Reynolds lead citrate and 15nm gold particles (BBI International) were affixed to the section surface to serve as fiducial markers for alignment.

Tomography was performed using a Tecnai F30 microscope operating at 300 kV (Thermo Fisher, Waltham MA). Dual-axis tilt series (+/-60˚, imaged every 1.5˚) were collected using SerialEM software[134] and a Gatan OneView camera at a pixel size of 1.5 nm. For most data sets, tilt series were collected from 2-3 serial sections in order to reconstruct the entire mitotic spindle in the tomographic volume. Serial tomograms were computed and joined using the IMOD 4.9 software package[136,159,160].

Spindle microtubules from either pole were tracked and their plus ends modeled using the 3dmod program of the IMOD software package. The spindles were then projected in 3D to show their arrangement within the volume. Measurements of spindle length, spindle microtubule length and diameter of spindle pole bodies were collected using the imodinfo program in the IMOD software package. In total, 6 complete spindles (ranging in length from 0.6 mm to 3.38 mm) and 3 half spindles from late anaphase were reconstructed.

3.6 Figures & legends

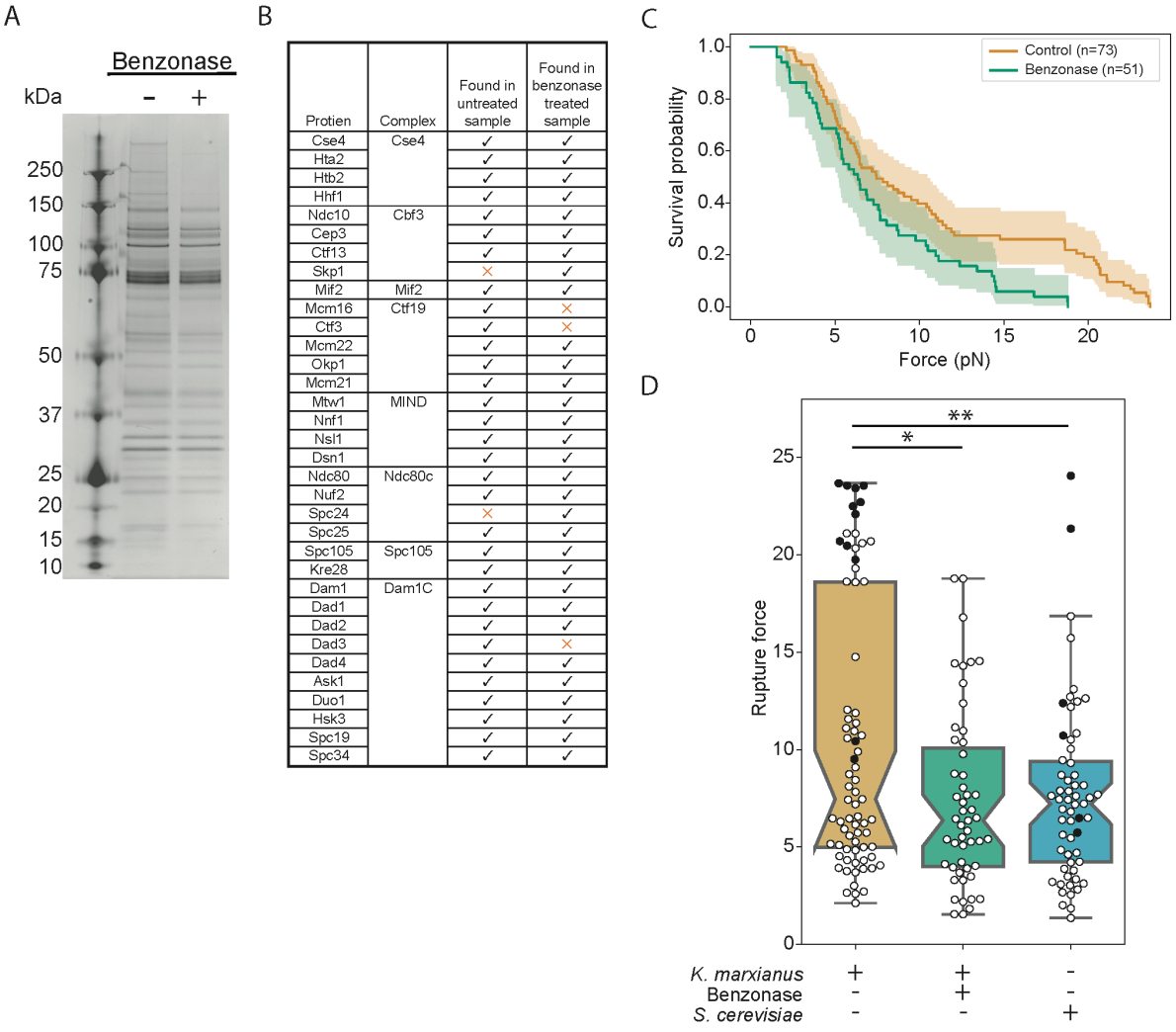

Protien	Complex	Found in untreated sample	Found in benzonase treated sample
Cse4	Cse4	✓	✓
Hta2		✓	✓
Htb2		✓	✓
Hhf1		✓	✓
Ndc10	Cbf3	✓	✓
Cep3		✓	✓
Ctf13		✓	✓
Skp1		×	✓
Mif2	Mif2	✓	✓
Mcm16	Ctf19	✓	×
Ctf3		✓	×
Mcm22		✓	✓
Okp1		✓	✓
Mcm21		✓	✓
Mtw1	MIND	✓	✓
Nnf1		✓	✓
Nsl1		✓	✓
Dsn1		✓	✓
Ndc80	Ndc80c	✓	✓
Nuf2		✓	✓
Spc24		×	✓
Spc25		✓	✓
Spc105	Spc105	✓	✓
Kre28		✓	✓
Dam1	Dam1C	✓	✓
Dad1		✓	✓
Dad2		✓	✓
Dad3		✓	×
Dad4		✓	✓
Ask1		✓	✓
Duo1		✓	✓
Hsk3		✓	✓
Spc19		✓	✓
Spc34		✓	✓

Figure 1. The loss of doublets does not significantly impact kinetochore composition, but affects strength. B) Kinetochores purified via Dsn1-6His-3M3DK (from strain SBY18150) visualized by silver stain with or without benzonase treatment. B) a representative mass spectrometry run of purified kinetochores with or without benzonase treatment. Checks indicate the protein was detected, orange Xs indicate it was not. C) Left: survival probability curves of force ramp experiments of untreated *K. marxianus* kinetochores (orange, median = 7.5 pN) and benzonase

treated *K. marxianus* kinetochores (green. median = 6.4 pN). Shaded regions represent the 95% confidence intervals. The survival curves differ significantly ($p < 0.005$ by log-rank test). D) Box plots of rupture force values overlayed with individual events for untreated *K. marxianus* (orange), benzonase treated *K. marxianus* (green), and untreated *S. cerevisiae* (blue, median = 7.2, log-rank test). White circles represent true ruptures and black circles represent escape events. Untreated and benzonase treated *K. marxianus* differed significantly ($p<0.005$, log-rank test), as did untreaded *K. marxianus* and untreated *S. cerevisiae* ($p=0.04$, log-rank test). Benzonase treated *K. marxianus* and untreated *S. cerevisiae* were indistinguishable ($p=0.77$, log-rank test).

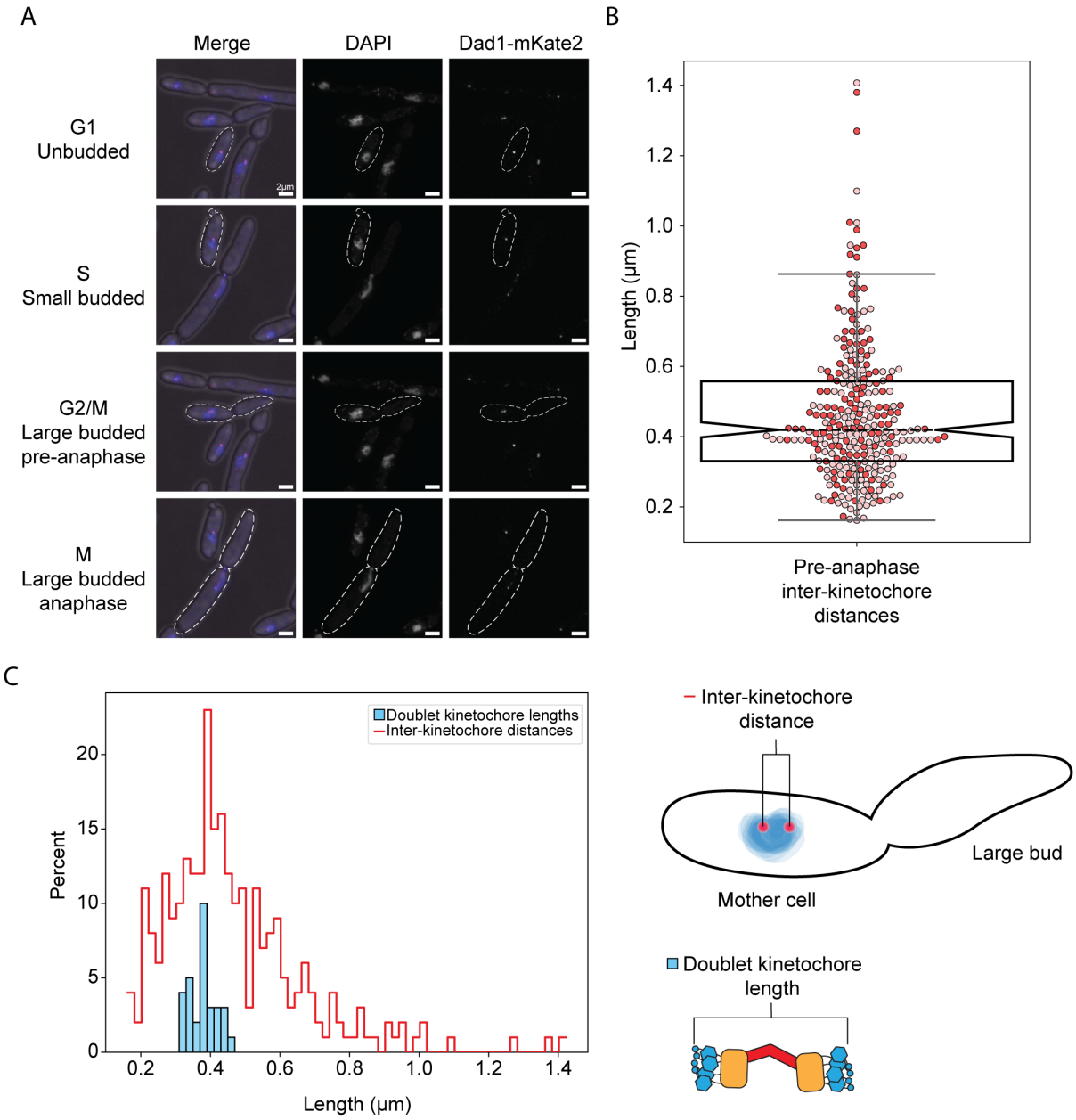

Figure 2. Kinetochores localize normally during cell cycle and are consistent with tomography measurements. A) Representative images of DAPI stained Dad1-mKate2 *K. marxianus* cells throughout the cell cycle, going from unbudded in the top row to large-budded and beginning anaphase in the bottom. Scale bar is 2 μm. B) Pre-anaphase Inter-kinetochore distances measured as the distance from the center of one Dad1-mKate2 focus to the center of the second (median = 0.42 μm, n = 274 distances from 2 biological replicates). Each circle is a

single measurement, colored by biological replicate, and the boxplot notch represents the median value. C) Left: A histogram comparison of the inter-kinetochore distance measured by fluorescence and the doublet kinetochore lengths previously measured by tomography[140], indicating that these two measurements are consistent. Right: cartoon schematics of the inter-kinetochore distance measurement (top) and the doublet kinetochore length measurement.

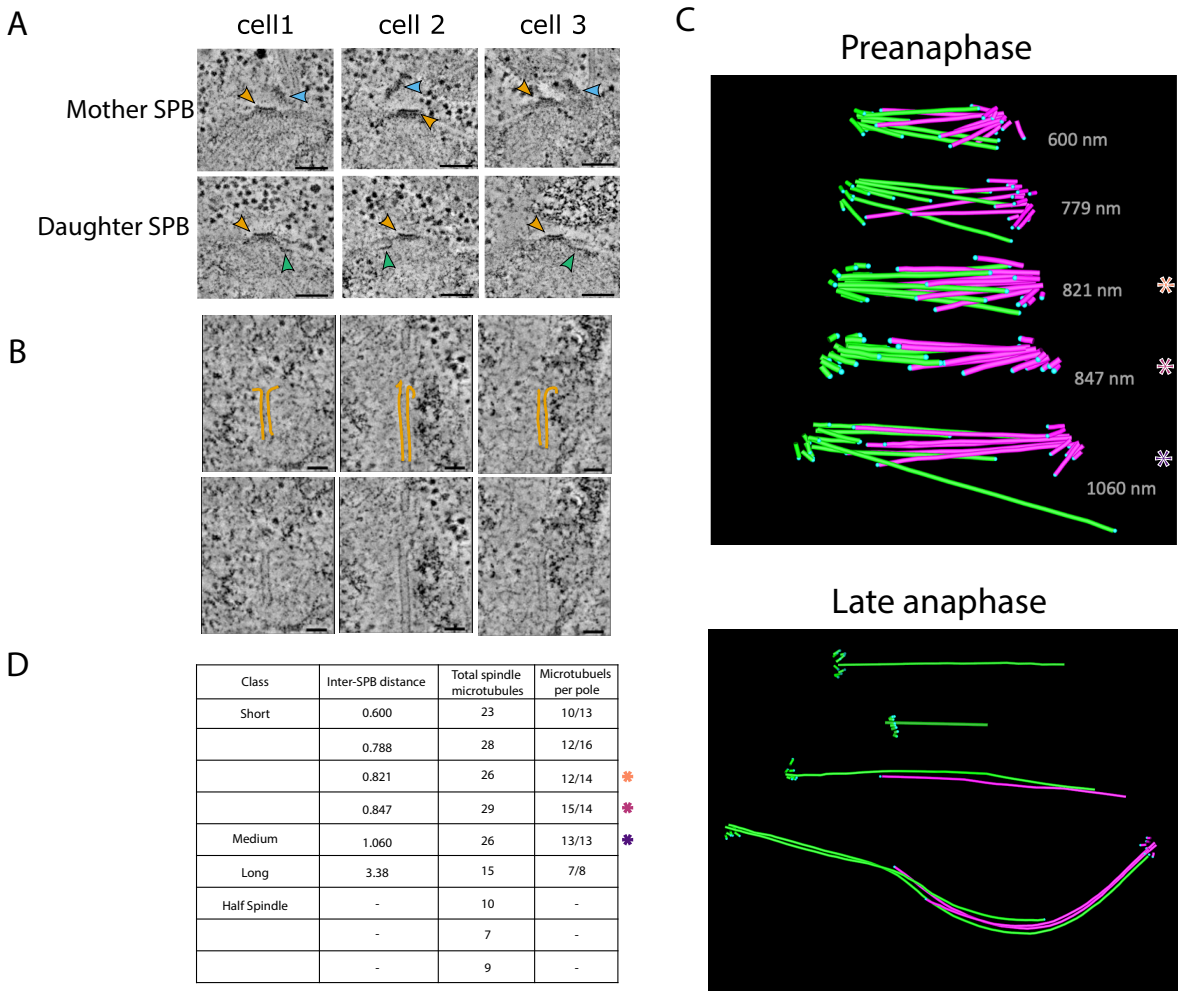

D

Class	Inter-SPB distance	Total spindle microtubules	Microtubuels per pole	
Short	0.600	23	10/13	
	0.788	28	12/16	
	0.821	26	12/14	*
	0.847	29	15/14	*
Medium	1.060	26	13/13	*
Long	3.38	15	7/8	
Half Spindle	-	10	-	
	-	7	-	
	-	9	-	

Figure 3. 3-dimensional reconstruction of *K. marxianus* mitotic spindles indicate a point centromere. A) An array of mother (top row) and daughter (bottom row) spindle pole bodies from three *K. marxianus* cells. Yellow arrows indicate the spindle pole bodies, blue arrows indicate the tilted outer plaques of mother SPBs. Half bridges are visible as a thin line of dark staining extending along the nuclear membrane (green arrows). B) Representative gallery of spindle microtubule tips. Protofilaments have been traced in yellow (top row), and unmarked images have been included for comparison (bottom row). C) Examples of reconstructed spindle models. Preanaphase spindles are shown on the left and late anaphase half spindles and a complete late anaphase spindle is shown on the right. Microtubules originating from the same SPB are

denoted in the same color, either pink or green. Length in nanometers from SPB to SPB are denoted by each spindle. Blue dots indicate the termination point of the microtubule. Scale bars represent 100 nanometers.

D) Classes, lengths, and microtubule content of reconstructed mitotic spindles. As length was measured from SPB to SPB, this measurement was omitted for half spindles where only one SPB was visible.

Chapter 4: Conclusions and future directions

4.1 Conclusions from this work

In the work showcased here I build on previous work characterizing native kinetochore particles by turning to the thermotolerant yeast *K. marxianus.* We first demonstrate that these particles are quite complete by mass spectrometry and immunoblot analysis. We also biophysically characterize these particles by assaying their ability to bind microtubules under force. The force needed to rupture these kinetochores from the microtubule shows a bimodal distribution, with one group centered similarly to *S. cerevisiae* and a second significantly stronger group. By negative stain EM the kinetochores appear larger than those reported for *S. cerevisiae* and exhibit a paintbrush like architecture; two spatially separated electron dense regions linked by strands, with a projection emerging from the smaller electron dense region. Kinetochores can also be seen linked through this projection, thus giving rise to two classes, singlets and doublets.

We next established the polarity of these particles by identifying the microtubule binding end and the DNA binding end. Nuclease treatment tended to separate doublets at the handles, indicating the presence of DNA in that region. Consistent with this and with the idea of a hierarchical assembly from DNA binding components to microtubule binders, the opposite end (i.e. the “brush”), was the microtubule binding region. Experiments visualizing kinetochores bound to taxol-stabilized microtubules showed a strong preference for binding to both the lattice and the tip with this region. Immuno-gold labeling further confirmed the presence of Ndc80 in the distal portion of the brush tips, establishing inner and outer kinetochore polarity in these particles.

To gain a higher resolution understanding of these particles we turned to cryo-electron tomography (cryo-ET). Using this method, we were able to better visualize the connections between the electron dense layers, the handle protrusion, and the microtubule binding domains.

The overall shape was consistent with the negative stain EM data and with atomic force microscopy (AFM) experiments. However, due to low particle abundance and high flexibility we were not able build high resolution electron density maps by sub-tomogram averaging. High-speed AFM experiments further confirmed the flexibility of these particles.

The presence of singlet and doublet kinetochores suggested the doublets were indicative a regional kinetochore. Because it is well established that other budding yeast utilize a point centromere, we sought to explore this further.

Our previous work had established a bimodal distribution in the rupture force data for *K. marxianus*, and that doublet kinetochores are linked by DNA consistent with a regional centromere. Disruption of the doublets by nuclease treatment eliminated the high strength rupture group, again suggesting there may be regional centromeres.

Because this would represent a significant difference from *S. cerevisiae*, we first wanted to understand if the cell cycle, and specifically kinetochore positioning through that cycle, was consistent between the two. Like *S. cerevisiae, K. marxianus* cells appeared to go through a similar budding cycle, and kinetochores remained assembled and localized to a single focus within the nucleus for much of the cell cycle, based on localization of the fluorophore tagged kinetochore component Dad1-mKate2. Additionally, measurements of in-vivo inter-kinetochore distances in cells pre anaphase mitotic cells indicated that both singlet and doublet kinetochores could fit within the spindle.

To determine the number of microtubule binding sites per centromere we reconstructed whole spindles from high-pressure frozen logarithmically growing cells. In these reconstructions we were able to localize the spindle pole bodies (SPBs) and trace individual microtubules from the SPBs to their plus ends. By counting the number of microtubules and comparing it to the number of chromosomes in our strain (8) we were able to determine that there were not enough microtubules to account for multiple microtubule binding sites per centromere.

4.1 Future directions

This work provided exciting glimpses at complete, native kinetochores, and improving on the tomography data will be an exciting area of work. Even short of averaging, using perturbations to test aspects of kinetochore organization will be illuminating. For instance, a prediction of this paper is that much of the density in the microtubule binding distal brush is due to Dam1c heterodecamers, which are associated with Ndc80c but not forming a ring. This could be interrogated by purifying kinetochores from a strain in which Dam1c can be disturbed such as with an inducible degron. If our prediction is correct, degradation of the Dam1c would eliminate substantial density from the distal brush. This same method could be applied to other regions of the kinetochore, including to interrogate the dense inner kinetochore region.

The most exciting possibility for tomographic work would be in-situ tomography. A fluorophore tagged kinetochore strain has already been generated for this work. This opens the possibility for correlated light and electron microscopy. Yeast with fluorophore tagged kinetochores could be deposited on electron microscopy grids and flash frozen. The kinetochores within these cells could then be localized by fluorescence signal and a focused ion beam used to mill a lamella on which a tomogram could be collected. Though it would be challenging to collect enough tomograms with visible kinetochores to average into a high resolution structure, it would give incredible insight as to the structure and organization of kinetochores in their native environment while they are functioning. In the coming years this is the direction I believe the kinetochore structural field will head.

Another interesting area to explore would be the assembly of these kinetochores. The development of a de-novo kinetochore assembly assay on short CEN DNA sequences has opened many avenues of experiments in *S. cerevisiae,* especially with regards to the temporal order of kinetochore assembly. Similar experiments are possible in *K. marxianus.* Even the first nucleosome wrapping step would be an interesting comparison. As previously stated, the

centromeric sequence of *K. marxianus* differs from *S. cerevisiae* in that CDEII is twice as long. While it does not appear that *K. marxianus* employs a regional centromere, this does suggest a difference at first step of kinetochore assembly.

The TIRF assembly assay could also be a powerful way to dissect the stoichiometry in these kinetochores. An initially surprising feature highlighted in *K. marxianus* kinetochores was their larger size. By labeling different components with fluorophores and performing assemblies on TIRF microscopy slides it would be possible to perform photobleaching experiments. This would allow for the determination of copy number for different components. A related and ongoing area of study within the lab is the development of FRET systems to monitor nucleosome wrapping in the context of the centromere. With its differing CDEII, *K. marxianus,* would offer and interesting point of comparison in these experiments. In summary, this work provides the foundation to study global kinetochore architecture at a structural level, and no shortage of future directions in which to run.

References

1 Jover, A. B. & Dekker, C. The archaeal Cdv cell division system. *Trends Microbiol* **31**, doi:10.1016/j.tim.2022.12.006 (2023).

2 Margolin, W. & Bernander, R. How do prokayrotic cells cycle? *Curr Biol.* **14**, doi:10.1016/j.cub.2004.09.017 (2004).

3 Flemming, W. *Zellsubstanz, Kern, und Zelltheilung*. (F.C.W. Vogel, 1882).

4 Gonçalves dos Santos Silva, A. *et al.* Centromeres in cell division, evolution, nuclear organization and disease. *J Cell Biochem.* **104**, doi:10.1002/jcb.21766 (2008).

5 Winey, M. & Bloom, K. Mitotic spindle form and function. *Genetics* **190**, 1197-1224 (2012).

6 Oakley, B. R., Oakley, C. E., Yoon, Y. & Jung, M. K. g-Tubulin is a component of the spindle pole body that is essential for mictrotubule function in *Aspergillus nidulans. Cell* **61**, 1289-1301 (1990).

7 Jaspersen, S. L. Anatomy of the fungal microtubule organizing center, the spindle pole body. *Curr Opin Cell Biol.* **66**, 22-31, doi:https://doi.org/10.1016/j.sbi.2020.09.008 (2021).

8 Byers, B. & Goetsch, L. Behavior of Spindle and Spindle Plaques in the Cell Cycle and Conjugation of *Saccharomyces cerevisiae*. *J. Bacteriol.* **124**, 511-523 (1975).

9 O'Toole, E. T., Winey, M. & McIntosh, J. R. High-voltage electron tomography of spindle pole bodies and early mitotic spindles in the yeast Saccharomyces cerevisiae. *Mol Biol Cell* **10**, 2017-2031 (1999).

10 Bullitt, E., Rout, M. P., Kilmartin, J. V. & Akey, C. W. The yeast spindle pole body is assembled around a central crystal of Spc42p. *Cell* **89**, 1077-1086, doi:https://doi.org/10.1016/S0092-8674(00)80295-0 (1997).

11 Adams, I. R. & Kilmartin, J. V. Localization of core spindle pole body (SPB) components during SPB duplication in Saccharomyces cerevisiae. *J Cell Biol* **145**, 809-823 (1999).

12 Muller, E. G. *et al.* The organization of the core proteins of the yeast spindle pole body. *Mol Biol Cell* **16**, 3341-3352 (2005).

13 Kollman, J. M. *et al.* The structure of the y-Tubulin small complex: implications of its architecture and flexibility for microtubule nucleation. *Mol. Biol. Cell* **19**, doi:https://doi.org/10.1091/mbc.e07-09-0879 (2007).

14 Kollman, J. M. *et al.* Ring closure activates yeast yTuRC for species-specific microtubule nucleation. *Nat Struct Mol Biol* **22**, 132-137, doi:https://doi.org/10.1038/nsmb.2953 (2015).

15 Winey, M. *et al.* Three-dimensional ultrastructural analysis of the *Saccharomyces cerevisiae* mitotic spindle. *J Cell Biol* **129**, 1601-1615 (1995).

16 Erlemann, S. *et al.* An extended y-Tubulin ring functions as a stable platform in microtubule nucleation. *J Cell Biol* **197**, 59-74, doi:https://doi.org/10.1083/jcb.201111123 (2012).

17 Lengefeld, J. *et al.* Spatial cues and not spindle pole maturation drive the asymmetry of astral microtubules between new and preexisting poles. *Mol. Biol. Cell* **29**, doi:https://doi.org/10.1091/mbc.E16-10-0725 (2018).

18 Cavanaugh, A. M. & Jaspersen, S. L. Big lessons from little yeast: budding and fission yeast centrosome structure, duplication, and function. *Annu. Rev. Genetic.* **51**, 361-383, doi:https://doi.org/10.1146/annurev-genet-120116-024733 (2017).
19 Byers, B. & Goetsch, L. Duplication of spindle plaques and integration of the yeast cell cycle. *Cold Spring Harbor Symp. Quant. Biol.* **38**, 123-131 (1974).
20 Avena, J. S. *et al.* Licensing of yeast centrosome duplication requires phosphoregulation of Sfi1. *PLOS Genet.*, doi:https://doi.org/10.1371/journal.pgen.1004666 (2014).
21 Burns, S. *et al.* Structured illumination with particle averaging reveals novel roles for yeast centrosome components during duplication. *eLife*, doi:https://doi.org/10.7554/eLife.08586 (2015).
22 Jaspersen, S. L. & Ghosh, S. nuclear envelope insertion of spindle pole bodies and nuclear pore complexes. *Nucleus* **3**, 226-236, doi:10.4161/nucl.20148 (2012).
23 Crasta, K., Huang, P., Morgan, G., Winey, M. & Surana, U. Cdk1 regulates centrosome separation by restraining proteolysis of microtubule-associated proteins. *Embo J* **25**, 2551-2563 (2006).
24 Hepperla, A. J. *et al.* Minus-end-directed kinesin-14 motors align antiparallel microtubules to control metaphase spindle length. *Dev. Cell.* **31**, 61-72, doi:https://doi.org/10.1016/j.devcel.2014.07.023 (2014).
25 Lansky, Z. *et al.* Diffusable crosslinkers generate directed forces in microtubule networks. *Cell* **160**, 1159-1168, doi:https://doi.org/10.1016/j.cell.2015.01.051 (2015).
26 Edelmaier, C. *et al.* Mechanisms of chromosome biorientation and bipolar spindle assembly analyzed by computational modeling. *eLife*, doi:https://doi.org/10.7554/eLife.48787 (2020).
27 Witman, G. B., Carlson, K., Berliner, J. & Rosenbaum, J. L. Chlamydomonas flagella. I. isolation and electrophoretic analysis of microtubules, matrix, membranes, and mastigonemes. *J Cell Biol.* **54**, 507-539, doi:10.1083/jcb.54.3.507 (1972).
28 Nogales, E., Whittaker, M., Milligan, R. A. & Downing, K. H. High-resolution model of the microtubule. *Cell* **96**, 79-88, doi:https://doi.org/10.1016/S0092-8674(00)80961-7 (1999).
29 Mitchison, T. & Kirschner, M. Dynamic instability of microtubule growth. *Nature* **312**, 237-242 (1984).
30 Mitchison, T. J. Microtubule dynamics and kinetochore function in mitosis. *Ann. Rev. Cell Biol.* **4**, 527-549 (1988).
31 Gudimchuk, N. B. & McIntosh, J. R. Regulation of microtubule dynamics, mechanics, and function through the growing tip. *Nat Rev Mol Cell Biol* **22**, 777-795, doi:https://doi.org/10.1038/s41580-021-00399-x (2021).
32 Ayukawa, R. *et al.* GTP-dependent formation of straight tubulin oligomers leads to microtubule nucleation. *J Cell Biol* **220**, doi:10.1083/jcb.202007033 (2021).
33 Nawrotek, A., Knossow, M. & Gigant, B. The determinants that govern microtubule assembly from the atomic structure of GTP tubulin. *J Mol Biol.* **412**, doi:10.1016/j.jmb.2011.07.029. (2011).

34 Buey, R. M., Díaz, J. F. & Andreu, J. M. The nucleotide switch of tubulin and microtubule assembly: a polymerization-driven structural change. *Biochemsitry* **45**, 5933-5938, doi:10.1021/bi060334m. (2006).
35 Musacchio, A. & Desai, A. A molecular view of kinetochore assembly and function. *Biology (Basel)* **6**, doi:10.3390/biology6010005 (2017).
36 Cheeseman, I. M. The kinetochore. *Cold Spring Harb Perspect Biol* **6**, a015826, doi:10.1101/cshperspect.a015826 (2014).
37 McAinsh, A. D. & Marston, A. L. The four causes: The functional architecture of centromeres and kinetochores. *Annu Rev Genet* **56**, 279-314, doi:10.1146/annurev-genet-072820-034559 (2022).
38 Clarke, L. Centromeres: proteins, protein complexes, and repeated domains at centromeres of simple eukaryotes. *Curr Opin Genet Dev* **8**, 212-218 (1998).
39 Burrack, L. S. & Berman, J. Flexibility of centromere and kinetochore structures. *Trends Genet.* **28**, 204-212, doi:10.1016/j.tig.2012.02.003. (2012).
40 Bloom, K. S. & Carbon, J. Yeast centromere DNA is in a unique and highly ordered structure in chromosomes and small circular minichromosomes. *Cell* **29**, 305-317 (1982).
41 Stoler, S., Keith, K. C., Curnick, K. E. & Fitzgerald-Hayes, M. A mutation in *CSE4*, an essential gene encoding a novel chromatin-associated protein in yeast, causes chromosome nondisjunction and cell cycle arrest at mitosis. *Genes Dev* **9**, 573-586 (1995).
42 Meluh, P. B., Yang, P., Glowczewski, L., Koshland, D. & Smith, M. M. Cse4p is a component of the core centromere of Saccharomyces cerevisiae. *Cell* **94**, 607-613 (1998).
43 Guan, R. *et al.* Structural and dynamic mechanisms of CBF3-guided centromeric nucleosome formation. *Nat Commun* **12**, 1763, doi:10.1038/s41467-021-21985-9 (2021).
44 Camahort, R. *et al.* Cse4 is part of an octameric nucleosome in budding yeast. *Mol Cell* **35**, 794-805, doi:10.1016/j.molcel.2009.07.022 (2009).
45 Migl, D. *et al.* Cryoelectron microscopy structure of a yeast centromeric nucleosome at 2.7 A resolution. *Structure* **28**, 363-370, doi:https://doi.org/10.1016/j.str.2019.12.002 (2020).
46 Popchock, A. R., Larson, J. D., Dubrulle, J., Asbury, C. L. & Biggins, S. Direct observation of coordinated assembly of individual native centromeric nucleosomes. *EMBO J.* **42**, doi:10.15252/embj.2023114534 (2023).
47 McAinsh, A. D. & Meraldi, P. The CCAN complex: linking centromere specification to control of kinetochore-microtubule dynamics. *Semin Cell Dev Biol* **22**, 946-952, doi:10.1016/j.semcdb.2011.09.016 (2011).
48 Pesenti, M. E. *et al.* Reconstitution of a 26-Subunit Human Kinetochore Reveals Cooperative Microtubule Binding by CENP-OPQUR and NDC80. *Mol Cell* **71**, 923-939 e910, doi:10.1016/j.molcel.2018.07.038 (2018).
49 Dendooven, T. *et al.* Cryo-Em structure of the complete inner kinetochore of the budding yeast point centromere. *Sci. Adv.* **9**, doi:10.1126/sciadv.adg7480 (2023).
50 Hinshaw, S. M. & Harrison, S. C. The structure of the Ctf19c/CCAN from budding yeast. *Elife* **8**, doi:10.7554/eLife.44239 (2019).

51 Pentakota, S. *et al.* Decoding the centromeric nucleosome through CENP-N. *Elife* **6**, doi:10.7554/eLife.33442 (2017).
52 Fischbock-Halwachs, J. *et al.* The COMA complex interacts with Cse4 and positions Sli15/Ipl1 at the budding yeast inner kinetochore. *Elife* **8**, doi:10.7554/eLife.42879 (2019).
53 Anedchenko, E. A. *et al.* The inner kinetochore module Okp1(Cenp-Q)/Ame1(Cenp-U) is a reader for N-terminal modifications on the centromeric histone Cse4(Cenp-A). *EMBO J.* **38**, doi:https://doi.org/10.15252/embj.201898991 (2018).
54 Yan, K. *et al.* Structure of the inner kinetochore CCAN complex assembled onto a centromeric nucleosome. *Nature* **574**, 278-282, doi:10.1038/s41586-019-1609-1 (2019).
55 Pekgoz Altunkaya, G. *et al.* CCAN Assembly Configures Composite Binding Interfaces to Promote Cross-Linking of Ndc80 Complexes at the Kinetochore. *Curr Biol* **26**, 2370-2378, doi:10.1016/j.cub.2016.07.005 (2016).
56 Takeuchi, K. *et al.* The centromeric nucleosome-like CENP-T-W-S-X complex induces positive supercoils into DNA. *Nucleic Acids Res*, doi:10.1093/nar/gkt1124 (2013).
57 Hinshaw, S. M. & Harrison, S. C. The Structural Basis for Kinetochore Stabilization by Cnn1/CENP-T. *Curr Biol* **30**, 3425-3431 e3423, doi:10.1016/j.cub.2020.06.024 (2020).
58 Joglekar, A. P., Bouck, D. C., Molk, J. N., Bloom, K. S. & Salmon, E. D. Molecular architecture of a kinetochore-microtubule attachment site. *Nat Cell Biol* **8**, 581-585, doi:10.1038/ncb1414 (2006).
59 Dimitrova, Y. N., Jenni, S., Valverde, R., Khin, Y. & Harrison, S. C. Structure of the MIND Complex Defines a Regulatory Focus for Yeast Kinetochore Assembly. *Cell* **167**, 1014-1027 e1012, doi:10.1016/j.cell.2016.10.011 (2016).
60 Petrovic, A. *et al.* Structure of the MIS12 Complex and Molecular Basis of Its Interaction with CENP-C at Human Kinetochores. *Cell* **167**, 1028-1040 e1015, doi:10.1016/j.cell.2016.10.005 (2016).
61 De Wulf, P., McAinsh, A. D. & Sorger, P. K. Hierarchical assembly of the budding yeast kinetochore from multiple subcomplexes. *Genes Dev* **17**, 2902-2921, doi:10.1101/gad.1144403 (2003).
62 Meeks-Wagner, D., Wood, J. S., Garvik, B. & Hartwell, L. H. Isolation of two genes that affect mitotic chromosome transmission in S. cerevisiae. *Cell* **44**, 53-63 (1986).
63 Hornung, P. *et al.* A cooperative mechanism drives budding yeast kinetochore assembly downstream of CENP-A. *J Cell Biol* **206**, 509-524, doi:10.1083/jcb.201403081 (2014).
64 Schleiffer, A. *et al.* CENP-T proteins are conserved centromere receptors of the Ndc80 complex. *Nat Cell Biol* **14**, 604-613, doi:10.1038/ncb2493 (2012).
65 Killinger, K. *et al.* Auto-inhibition of Mif2/Cenp-C ensures centromere-dependent kinetochore assembly in budding yeast. *EMBO J.* **39**, doi:https://doi.org/10.15252/embj.2019102938 (2020).

66 Lang, J., Barber, A. & Biggins, S. An assay for de novo kinetochore assembly reveals a key role for the CENP-T pathway in budding yeast. *Elife* **7**, doi:10.7554/eLife.37819 (2018).
67 Wang, H. W. *et al.* Architecture and flexibility of the yeast Ndc80 kinetochore complex. *J Mol Biol* **383**, 894-903, doi:10.1016/j.jmb.2008.08.077 (2008).
68 Wei, R. R., Sorger, P. K. & Harrison, S. C. Molecular organization of the Ndc80 complex, an essential kinetochore component. *Proc Natl Acad Sci U S A* **102**, 5363-5367, doi:10.1073/pnas.0501168102 (2005).
69 Wei, R. R. *et al.* Structure of a central component of the yeast kinetochore: the Spc24p/Spc25p globular domain. *Structure* **14**, 1003-1009, doi:10.1016/j.str.2006.04.007 (2006).
70 Wei, R. R., Al-Bassam, J. & Harrison, S. C. The Ndc80/HEC1 complex is a contact point for kinetochore-microtubule attachment. *Nat Struct Mol Biol* **14**, 54-59, doi:10.1038/nsmb1186 (2007).
71 Ciferri, C. *et al.* Implications for kinetochore-microtubule attachment from the structure of an engineered Ndc80 complex. *Cell* **133**, 427-439, doi:10.1016/j.cell.2008.03.020 (2008).
72 Alushin, G. M. *et al.* The Ndc80 kinetochore complex forms oligomeric arrays along microtubules. *Nature* **467**, 805-810, doi:10.1038/nature09423 (2010).
73 Akiyoshi, B., Nelson, C. R., Ranish, J. A. & Biggins, S. Analysis of Ipl1-mediated phosphorylation of the Ndc80 kinetochore protein in *Saccharomyces cerevisiae*. *Genetics* **183**, 1591-1595, doi:10.1534/genetics.109.109041 (2009).
74 Polley, S. *et al.* Insights into human outer kinetochore assembly and force transmission from a structure-function analysis of the KMN network. *bioRxiv*, doi:https://doi.org/10.1101/2023.08.07.552315 (2023).
75 Yatskevich, S., Yang, J., Bellini, D., Zhang, Z. & Barford, D. Structure of the human outer kinetochore KMN network complex. *Nat Struct Mol Biol*, doi:https://doi.org/10.1038/s41594-024-01249-y (2024).
76 Petrovic, A. *et al.* Modular assembly of RWD domains on the Mis12 complex underlies outer kinetochore organization. *Mol Cell* **53**, 591-605, doi:10.1016/j.molcel.2014.01.019 (2014).
77 London, N., Ceto, S., Ranish, J. A. & Biggins, S. Phosphoregulation of Spc105 by Mps1 and PP1 regulates Bub1 localization to kinetochores. *Curr Biol* **22**, 900-906, doi:10.1016/j.cub.2012.03.052 (2012).
78 London, N. & Biggins, S. Mad1 kinetochore recruitment by Mps1-mediated phosphorylation of Bub1 signals the spindle checkpoint. *Genes Dev* **28**, 140-152, doi:10.1101/gad.233700.113 (2014).
79 Biggins, S. The composition, functions, and regulation of the budding yeast kinetochore. *Genetics* **194**, 817-846, doi:10.1534/genetics.112.145276 (2013).
80 Nogales, E. & Ramey, V. H. Structure-function insights into the yeast Dam1 kinetochore complex. *J Cell Sci* **122**, 3831-3836, doi:10.1242/jcs.004689 (2009).
81 Jenni, S. & Harrison, S. C. Structure of the DASH/Dam1 complex shows its role at the yeast kinetochore-microtubule interface. *Science* **360**, 552-558, doi:10.1126/science.aar6436 (2018).

82 Miranda, J. J., De Wulf, P., Sorger, P. K. & Harrison, S. C. The yeast DASH complex forms closed rings on microtubules. *Nat Struct Mol Biol* **12**, 138-143 (2005).
83 Westermann, S. *et al.* Formation of a dynamic kinetochore- microtubule interface through assembly of the Dam1 ring complex. *Mol Cell* **17**, 277-290, doi:10.1016/j.molcel.2004.12.019 (2005).
84 Ng, C. T. *et al.* Electron cryotomography analysis of Dam1C/DASH at the kinetochore-spindle interface in situ. *J. Cell Biol.* **218**, 455-473, doi:https://doi.org/10.1083/jcb.201809088 (2019).
85 Zahm, J. A., Jenni, S. & Harrison, S. C. Structure of the Ndc80 complex and its interactions at the yeast kinetochore-microtubule interface. *Open Biol.* **13**, doi:https://doi.org/10.1098/rsob.220378 (2023).
86 Akiyoshi, B. *et al.* Tension directly stabilizes reconstituted kinetochore-microtubule attachments. *Nature* **468**, 576-579 (2010).
87 Miller, M. P., Asbury, C. L. & Biggins, S. A TOG protein confers tension sensitivity to kinetochore-microtubule attachments. *Cell* **165**, 1428-1439, doi:10.1016/j.cell.2016.04.030 (2016).
88 Zahm, J. A., Stewart, M. G., Carrier, J. S., Harrison, S. C. & Miller, M. P. Structural basis of Stu2 recruitment to yeast kinetochores. *Elife* **10**, doi:10.7554/eLife.65389 (2021).
89 Doodhi, H. & Tanaka, T. U. Swap and stop - Kinetochores play error correction with microtubules: Mechanisms of kinetochore-microtubule error correction: Mechanisms of kinetochore-microtubule error correction. *Bioessays* **44**, e2100246, doi:10.1002/bies.202100246 (2022).
90 Miller, M. *et al.* A Stu2-mediated intrinsic tension-sensing pathway promotes chromosome biorientation in vivo. *PLOS Genet.*, doi:https://doi.org/10.1371/journal.pgen.1008423 (2019).
91 de Regt, A., Clark, C., Asbury, C. & Biggins, S. Tension can directly suppress Aurora B kinase-triggered release of kinetochore-microtubule attachments. *Nat Commun* **13**, 1-8, doi:https://doi.org/10.1038/s41467-022-29542-8 (2021).
92 Gonen, S. *et al.* The structure of purified kinetochores reveals multiple microtubule-attachment sites. *Nature Structural & Molecular Biology* **19**, 925-929, doi:10.1038/nsmb.2358 (2012).
93 Sundararajan, K. & Straight, A. F. Centromere identity and the regulation of chromosome segregation. *Front Cell Dev Biol*, doi:10.3389/fcell.2022.914249 (2022).
94 Kixmoeller, K., Allu, P. K. & Black, B. E. The centromere comes into focus: from CENP-A nucleosomes to kinetochore connections with the spindle. *Open Biol* **10**, 200051, doi:10.1098/rsob.200051 (2020).
95 Monda, J. K. & Cheeseman, I. M. The kinetochore-microtubule interface at a glance. *J Cell Sci* **131**, doi:10.1242/jcs.214577 (2018).
96 Foltz, D. R. *et al.* The human CENP-A centromeric nucleosome-associated complex. *Nat Cell Biol* **8**, 458-469 (2006).
97 Ariyoshi, M. & Fukagawa, T. An updated view of the kinetochore architecture. *Trends Genet* **39**, 941-953, doi:10.1016/j.tig.2023.09.003 (2023).

98 Yatskevich, S., Barford, D. & Muir, K. W. Conserved and divergent mechanisms of inner kinetochore assembly onto centromeric chromatin. *Curr Opin Struct Biol* **81**, 102638, doi:10.1016/j.sbi.2023.102638 (2023).
99 Cheeseman, I. M., Chappie, J. S., Wilson-Kubalek, E. M. & Desai, A. The conserved KMN network constitutes the core microtubule-binding site of the kinetochore. *Cell* **127**, 983-997, doi:10.1016/j.cell.2006.09.039 (2006).
100 DeLuca, J. G. *et al.* Kinetochore microtubule dynamics and attachment stability are regulated by Hec1. *Cell* **127**, 969-982, doi:10.1016/j.cell.2006.09.047 (2006).
101 Chen, G. Y. *et al.* Tension promotes kinetochore-microtubule release by Aurora B kinase. *J Cell Biol* **220**, doi:10.1083/jcb.202007030 (2021).
102 McAinsh, A. D. & Kops, G. Principles and dynamics of spindle assembly checkpoint signalling. *Nat Rev Mol Cell Biol* **24**, 543-559, doi:10.1038/s41580-023-00593-z (2023).
103 Furuyama, S. & Biggins, S. Centromere identity is specified by a single centromeric nucleosome in budding yeast. *Proc Natl Acad Sci U S A* **104**, 14706-14711, doi:10.1073/pnas.0706985104 (2007).
104 Hamilton, G., Dimitrova, Y. & Davis, T. N. Seeing is believing: our evolving view of kinetochore structure, composition, and assembly. *Curr Opin Cell Biol* **60**, 44-52, doi:10.1016/j.ceb.2019.03.016 (2019).
105 Pesenti, M. E. *et al.* Structure of the human inner kinetochore CCAN complex and its significance for human centromere organization. *Molecular Cell* **82**, 2113-2131, doi:https://doi.org/10.1016/j.molcel.2022.04.027 (2022).
106 Yatskevich, S. *et al.* Structure of the human inner kinetochore bound to a centromeric CENP-A nucleosome. *Science* **376**, 844-852, doi:10.1126/science.abn3810 (2022).
107 Kale, S. *et al.* The CENP-A nucleosome: where and when it happens during the inner kinetochore's assembly. *Trends Biochem Sci* **48**, 849-859, doi:10.1016/j.tibs.2023.07.010 (2023).
108 Valverde, R., Ingram, J. & Harrison, S. C. Conserved Tetramer Junction in the Kinetochore Ndc80 Complex. *Cell Rep* **17**, 1915-1922, doi:10.1016/j.celrep.2016.10.065 (2016).
109 Ciferri, C., Musacchio, A. & Petrovic, A. The Ndc80 complex: hub of kinetochore activity. *FEBS Lett* **581**, 2862-2869 (2007).
110 Muir, K. W. *et al.* Structural mechanism of outer kinetochore Dam1-Ndc80 complex assembly on microtubules. *Science* **328**, doi:10.1126/science.adj8736 (2023).
111 Malvezzi, F. *et al.* A structural basis for kinetochore recruitment of the Ndc80 complex via two distinct centromere receptors. *EMBO J* **32**, 409-423, doi:10.1038/emboj.2012.356 (2013).
112 Bock, L. J. *et al.* Cnn1 inhibits the interactions between the KMN complexes of the yeast kinetochore. *Nat Cell Biol* **14**, 614-624, doi:10.1038/ncb2495 (2012).
113 Joglekar, A. P., Bloom, K. & Salmon, E. D. In vivo protein architecture of the eukaryotic kinetochore with nanometer scale accuracy. *Curr Biol* **19**, 694-699, doi:10.1016/j.cub.2009.02.056 (2009).
114 Johnston, K. *et al.* Vertebrate kinetochore protein architecture: protein copy number. *J Cell Biol* **189**, 937-943, doi:10.1083/jcb.200912022 (2010).

115 Lawrimore, J., Bloom, K. S. & Salmon, E. D. Point centromeres contain more than a single centromere-specific Cse4 (CENP-A) nucleosome. *J Cell Biol* **195**, 573-582, doi:10.1083/jcb.201106036 (2011).
116 Dhatchinamoorthy, K. *et al.* Structural plasticity of the living kinetochore. *J Cell Biol* **216**, 3551-3570, doi:10.1083/jcb.201703152 (2017).
117 Bonner, M. K. *et al.* Enrichment of Aurora B kinase at the inner kinetochore controls outer kinetochore assembly. *J Cell Biol* **218**, 3237-3257, doi:10.1083/jcb.201901004 (2019).
118 Sarangapani, K. K., Koch, L. B., Nelson, C. R., Asbury, C. L. & Biggins, S. Kinetochore-bound Mps1 regulates kinetochore-microtubule attachments via Ndc80 phosphorylation. *J Cell Biol.* **220**, doi:https://doi.org/10.1083/jcb.202106130 (2021).
119 Torvi, J. R. *et al.* Reconstitution of kinetochore motility and microtubule dynamics reveals a role for a kinesin-8 in establishing end-on attachments. *eLife* **0:e78450**, doi:https://doi.org/10.7554/eLife.78450 (2022).
120 Meruelo, A., Han, S. K., Kim, S. & Bowie, J. U. Structural differences between thermophilic and mesophilic membrain proteins. *Protein Science* **21**, 1746-1753, doi:10.1002/pro.2157 (2012).
121 Szilágyi, A. & Závodsky, P. Structural differences between mesophilic, moderately thermophilic and extremely thermophilic protein subunits: results of a comprehensive survey. *Structure* **8**, 493-504, doi:https://doi.org/10.1016/S0969-2126(00)00133-7 (2000).
122 Amlacher, S. *et al.* Insight into Structure and Assembly of the Nuclear Pore Complex by Utilizing the genome of a Eukaryotic Thermophile. *Cell* **146**, 277-289 (2011).
123 Ghosh, S. K., Sau, S., Lahiri, S., Lohia, A. & Sinha, P. The Iml3 protein of the budding yeast is required for the prevention of precocious sister chromatid separation in meiosis I and for sister chromatid disjunction in meiosis II. *Curr Genet* **46**, 82-91, doi:10.1007/s00294-004-0516-6 (2004).
124 Nekrasov, V. S., Smith, M. A., Peak-Chew, S. & Kilmartin, J. V. Interactions between centromere complexes in *Saccharomyces cerevisiae*. *Mol Biol Cell* **14**, 4931-4946 (2003).
125 Arimura, Y., Konishi, H. A. & Funabiki, H. Cryo-EM analysis on magnetic beads for scarce macromolecules in heterogeneous samples. *bioRxiv*, doi:https://doi.org/10.1101/2024.01.21.576499 (2024).
126 Zhang, L. *et al.* An optimized negative-staining protocol of electron microscopy for apoE4 POPC lipoprotein. *J Lipid Res.* **51**, 1228-1236, doi:10.1194/jlr.D002493 (2010).
127 Jentink, N., Purnell, C., Kable, B., Swulius, M. T. & Grigoryev, S. A. Cryoelectron tomography reveals the multiplex anatomy of condensed native chromatin and its unfolding by histone citrullination. *Molecular Cell* **83**, 1-17 (2023).
128 Parnell, E. J., Jenson, E. & Miller, M. P. A conserved site on Ndc80 complex facilitates dynamic recruitment of Mps1 to yeast kinetochores to promote accurate chromosome segregation. *Curr Biol.* **34**, 1-14, doi:https://doi.org/10.1016/j.cub.2024.04.054 (2024).

129 Petrovic, A. *et al.* The MIS12 complex is a protein interaction hub for outer kinetochore assembly. *J Cell Biol* **190**, 835-852, doi:10.1083/jcb.201002070 (2010).
130 Iborra, F. & Ball, M. M. Kluyvermyces marxianus small DNA fragments contain both autonomous replicative and centromeric elements that also function in Kluyveromyces lactis. *Yeast* **10**, 1621-1629 (1994).
131 Brinkley, B. R. & Stubblefield, E. The fine structure of the kinetochore of a mammalian cell in vitro. *Chromosoma* **19**, 28-43 (1966).
132 Jokelainen, P. T. The ultrastructure and spatial organization of the metaphase kinetochore in mitotic rat cells. *J Ultrastruct Res* **19**, 19-44 (1967).
133 McEwen, B. F., Hsieh, C. E., Mattheyses, A. L. & Rieder, C. L. A new look at kinetochore structure in vertebrate somatic cells using high-pressure freezing and freeze substitution. *Chromosoma* **107**, 366-375 (1998).
134 Mastronarde, D. N. Automated electron microscope tomography using robust prediction of specimen movements. *J. Struct. Biol.* **152(1)**, 36-51 (2005).
135 Scheres, S. H. W. RELION: Implementation of a Bayesian approach to cryo-EM structure determination. *J. Struct. Biol.* **180(3)**, 519-530 (2012).
136 Mastronarde, D. N. & Held, S. R. Automated tilt series alignment and tomographic reconstruction in IMOD. *J. Struct. Biol.* **197(2)**, 102-113 (2017).
137 Agulleiro, J.-I. & Fernandez, J.-J. Tomo3d2.0 - Exploitation of Advanced Vector eXtensions (AVX) for 3D reconstruction. *J. Struct. Biol.* **189(2)**, 147-152 (2015).
138 Liu, Y. *et al.* Isotropic reconstruction for electron tomography with deep learning. *Nat. Commun.* **13 (6482)** (2022).
139 Miridita, M. *et al.* ColabFold: making protein folding accesible to all. *Nature Methods* **19**, 679-682, doi:https://doi.org/10.1038/s41592-022-01488-1 (2022).
140 Barrero, D. J. *et al.* Architecture and flexibility of native kinetochores revealed by structural studies utilizing a thermophilic yeast. *bioRxiv*, doi:https://doi.org/10.1101/2024.02.28.582571 (2024).
141 Hanahan, D. & Weinberg, R. A. Hallmarks of cancer: the next generation. *Cell* **144**, 646-674, doi:10.1016/j.cell.2011.02.013 (2011).
142 Pfau, S. J. & Amon, A. Chromosomal instability and aneuploidy in cancer: from yeast to man. *EMBO Rep* **13**, 515-527, doi:10.1038/embor.2012.65 (2012).
143 Klaasen, S. J. & Kops, G. J. P. L. Chromosome inequality: causes and consequence of non-random segregation errors in mitosis and meiosis. *Cells* **11**, doi:10.3390/cells11223564 (2022).
144 Palmer, D. K., O'Day, K., Wener, M. H., Andrews, B. S. & Margolis, R. L. A 17-kD centromere protein (CENP-A) copurifies with nucleosome core particles and with histones. *J Cell Biol* **104**, 805-815 (1987).
145 Long, A. F., Kuhn, J. & Dumont, S. The mammalian kinetochore-microtubule interface: robust mechanics and computation with many microtubules. *Curr Opin Cell Biol.*, doi:10.1016/j.ceb.2019.04.004 (2020).
146 Wigge, P. A. & Kilmartin, J. V. The Ndc80p complex from *Saccharomyces cerevisiae* contains conserved centromere components and has a function in chromosome segregation. *J Cell Biol* **152**, 349-360 (2001).

147 Kale, S. *et al.* The CENP-A nucleosome: where and when it happens during the inner kinetochore's assembly. *Trends Biochem Sci.* **48**, 849-859, doi:10.1016/j.tibs.2023.07.010. (2023).
148 Screpanti, E. *et al.* Direct binding of Cenp-C to the Mis12 complex joins the inner and outer kinetochore. *Curr Biol* **21**, 391-398, doi:10.1016/j.cub.2010.12.039 (2011).
149 Cieslinski, K. *et al.* Nanoscale structural organization and stoichiometry of the budding yeast kinetochore. *J Cell Biol* **222**, doi:https://doi.org/10.1083/jcb.202209094 (2023).
150 Kitamura, E., Tanaka, K., Kitamura, Y. & Tanaka, T. U. Kinetochore microtubule interaction during S phase in *Saccharomyces cerevisiae*. *Genes Dev* **21**, 3319-3330, doi:10.1101/gad.449407 (2007).
151 Kilmartin, J. V. Lessons from yeast: the spindle pole body and the centrosome. *Philos Trans R Soc Lond B Biol Sci* **369**, doi:10.1098/rstb.2013.0456 (2014).
152 O'Toole, E. T. *et al.* Three-dimensional analysis and ultrastructural design of mitotic spindles from the cdc20 mutant of Saccharomyces cerevisiae. *Mol Biol Cell* **8**, 1-11 (1997).
153 O'Toole, E. T., Giddings Jr, T. H. & Winey, M. Cryoprepartation and electron tomography of yeast cells. *Cold Spring Harb Protoc.* **2017(3)**, doi:10.1101/pdb.prot085589 (2017).
154 Storchova, Z. *et al.* Genome-wide genetic analysis of polyploidy in yeast. *Nature* **443**, 541-547, doi:10.1038/nature05178 (2006).
155 Nambu-Nishida, Y., Nishida, K., Hasunuma, T. & Akihiko, K. Development of a comprehensive set of tools for genome engineering in a cold- and thermo-tolerant Kluyveromyces marxianus yeast strain. *Sci Rep.* **7**, doi:10.1038/s41598-017-08356-5 (2017).
156 Skinner, S. O., Sepúlveda, L. A., Xu, H. & Golding, I. Measuring mRNA copy number in individual Escherichia coli cells using single-molecule fluorescent in situ hybridization. *Nat Protoc.* **8**, 110-1113, doi:https://doi.org/10.1038/nprot.2013.066 (2013).
157 Giddings Jr, T. H. *et al.* Using rapid freeze and freeze-substitution for the preparation of yeast cells for electron microscopy and three dimensional analysis. *Methods Cell Biol.* **67**, 27-42, doi:10.1016/s0091-679x(01)67003-1 (2001).
158 O'Toole, E., Giddings Jr, T. H. & Winey, M. Cryopreparation and electron tomography of yeast cells. *Cold Spring Harb Protoc.*, doi:10.1101/pdb.prot085589 (2017).
159 Kremer, J. R., Mastronarde, D. N. & McIntosh, J. R. Computer visualization of three-dimensional image data using IMOD. *J Struct Biol* **116**, 71-76, doi:10.1006/jsbi.1996.0013 (1996).
160 Mastronarde, D. N. Dual-axis tomography: an approach with alignment methods that preserve resolution. *J Struct Biol* **120**, 343-352, doi:10.1006/jsbi.1997.3919 (1997).